NSWC/WOL/TR 76-71

NSWC
TECHNICAL REPORT

WHITE OAK LABORATORY

BOUNDARY-LAYER TRANSITION EXPERIMENTS ON PRE-ABLATED GRAPHITE NOSETIPS
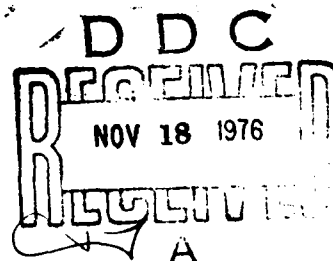IN A HYPERBALLISTICS RANGE

BY
Daniel C. Reda
Robert A. Leverance   30 JUNE 1976

NAVAL SURFACE WEAPONS CENTER
WHITE OAK LABORATORY
SILVER SPRING, MARYLAND 20910

● Approved for public release; distribution unlimited

NAVAL SURFACE WEAPONS CENTER
WHITE OAK, SILVER SPRING, MARYLAND 20910

REPORT DOCUMENTATION PAGE		READ INSTRUCTIONS BEFORE COMPLETING FORM
1. REPORT NUMBER NSWC/WOL/TR 76-71	2. GOVT ACCESSION NO.	3. RECIPIENT'S CATALOG NUMBER
4. TITLE *(and Subtitle)* Boundary-Layer Transition Experiments on Pre-ablated Graphite Nosetips in a Hyperballistics Range.		5. TYPE OF REPORT & PERIOD COVERED Final: 6/74-6/76
		6. PERFORMING ORG. REPORT NUMBER
7. AUTHOR(s) Daniel C. /Reda Robert A. /Leverance		8. CONTRACT OR GRANT NUMBER(s) F32322
9. PERFORMING ORGANIZATION NAME AND ADDRESS Naval Surface Weapons Center White Oak Laboratory White Oak, Silver Spring, Maryland 20910		10. PROGRAM ELEMENT, PROJECT, TASK AREA & WORK UNIT NUMBERS 62332N; F32322 SF32322501; WA2301
11. CONTROLLING OFFICE NAME AND ADDRESS		12. REPORT DATE 30 June 1976
		13. NUMBER OF PAGES 75
14. MONITORING AGENCY NAME & ADDRESS*(if different from Controlling Office)* 78 p.		15. SECURITY CLASS. *(of this report)* Unclassified
		15a. DECLASSIFICATION/DOWNGRADING SCHEDULE

16. DISTRIBUTION STATEMENT *(of this Report)*

Approved for public release; distribution unlimited

17. DISTRIBUTION STATEMENT *(of the abstract entered in Block 20, if different from Report)*

Final rpt. Jun 74 - Jun 76,

18. SUPPLEMENTARY NOTES

19. KEY WORDS *(Continue on reverse side if necessary and identify by block number)*

Reentry vehicle nosetips
Boundary-layer transition
Surface roughness effects
Aerodynamic heat transfer

20. ABSTRACT *(Continue on reverse side if necessary and identify by block number)*

An experimental program was conducted to test the validity of extrapolating the PANT (Passive Nosetip Technology) boundary-layer transition correlation, based on wind-tunnel/calorimeter-model results, to actual nosetip materials exposed to actual reentry environments. Pre-ablated ATJ-S graphite nosetips were flown on specific ballistics range trajectories through both air and nitrogen (with and without ablation). Surface temperature contours were measured via electro-optical pyrometry, from which transition zone presence and location were inferred. Significant discrepancies were noted between predicted and

experimentally observed transition zone behavior, as influenced by Reynolds number and wall-temperature effects. A question was raised concerning characterization of a surface microroughness distribution, for transition purposes, by its median value. In addition, significant surface roughness effects on laminar-flow heat-transfer rates were noted.

NSWC/WOL/TR 76-71   30 June 1976

BOUNDARY-LAYER TRANSITION EXPERIMENTS ON PRE-ABLATED GRAPHITE
NOSETIPS IN A HYPERBALLISTICS RANGE

This report outlines requirements and techniques for conducting
aerothermodynamic tests of reentry vehicle nosetips/materials
under controlled reentry environments in a hyperballistics range.
Using this capability, an experimental program was conducted to
test the validity of extrapolating an existing nosetip boundary-
layer transition correlation, based on wind-tunnel/calorimeter-
model results, to actual nosetip materials exposed to actual
reentry environments. Under such conditions, significant dis-
crepancies were noted between predicted and experimentally
observed transition zone behavior.

K. R. ENKENHUS
By direction

TABLE OF CONTENTS

ILLUSTRATIONS

TABLE

LIST OF SYMBOLS

B'	nondimensional blowing rate, $[\dot{m}_w/\rho_e V_e C_H]$
C	speed of sound
C_H	Stanton number
$E_b(\lambda)$	black body radiation
$E_G(\lambda,T,\rho)$	gas radiation
H	enthalpy
k	surface roughness height; for ablated material, represents numerical value used to characterize microroughness distribution
$k_{.5}, k_{.2}$	50, 20 percent of all roughness elements in distribution possess heights greater than this value
K_L	ratio of rough-to-smooth wall laminar heat-transfer rate
$\dot{m}$	mass addition rate per unit area
M	Mach number
P	pressure
Re_θ	momentum thickness Reynolds number, $\dfrac{\rho_e V_e \theta}{\mu_e}$
Re_∞/ft	freestream unit Reynolds number, $\dfrac{\rho_\infty V_\infty}{\mu_\infty}$
R_N	nosetip radius
R'_N	effective nosetip radius after ablation
S	arc length measured from geometric stagnation point
$S_{11}(\lambda), S_{20}(\lambda)$	image converter tube response
T	temperature
t	time of flight from muzzle exit
V	velocity
$W_{12}(\lambda)$	cut-off filter response
β	ballistic coefficient
$\Delta(\psi, V_\infty, P_\infty, R_N)$	local shock stand-off distance
Δr	recession normal to surface
δ^*	smooth-wall boundary-layer mass displacement thickness
ε	surface emissivity
θ	smooth-wall boundary-layer momentum thickness
λ	wavelength
μ	viscosity
ρ	density
Ψ'	local function of B', $\left(\dfrac{\rho_e}{\rho_w}\right)$
Ψ	angle measured from geometric stagnation point

Subscripts

e	at boundary-layer edge
i	at muzzle exit
SONIC	at sonic point
STAG	at stagnation point
TANK, RANGE	in blast tank, range
TR	at transition point
w	at wall or surface
∞	free stream
2	behind normal shock

I   INTRODUCTION

Strategic system reentry vehicles rely on passive ablating nosetips and heatshields for thermal protection. Nosetip materials of current interest are comprised of carbon, i.e., the polycrystalline graphites and the more recently developed carbon/carbon derivatives (carbon fiber bundles woven into a matrix, impregnated with a carbon filler material). These materials sublime under the severe aerothermodynamic environments of reentry, their mass loss (ablation) rate and shape change history dependent primarily on a complex interaction between ablated material surface roughness and the viscous flow (boundary layer) which develops over the surface.

Figure 1 schematically depicts nosetip shape change events which occur during clear-air reentry. Under high altitude/low freestream density conditions a nosetip experiences laminar ablation. An initially hemispherical contour is further blunted, with maximum recession occurring at the stagnation point (for zero angle-of-attack trajectories). This ablation process replaces the near-uniform surface roughness of the material, imposed by manufacturing/machining specifications, with a microroughness, k, characteristic of the nosetip material and independent of the trajectory flown. It is this microroughness which eventually trips the nosetip boundary layer to a turbulent state. Boundary-layer transition to turbulence results in more severe heat-transfer rates, increased ablation rates, accelerated shape change, and the formation of an increased macroroughness scale downstream of transition (e.g., striations, grooves, and/or scallops). Macroroughness element dimensions are dependent on both material and trajectory parameters as well as elapsed time of flight.

Design of advanced reentry vehicle nosetips requires a detailed understanding of viscous and inviscid flow fields, heat transfer, and ablation phenomena (shape change) within hypersonic real-gas environments. Computer codes used for such design calculations must accurately model such key elements as boundary-layer transition onset conditions, transition zone location and extent, roughness augmented heat transfer, and ablation thermochemistry.

Experimental information required for the correct modeling of such complex phenomena is often generated under wind-tunnel and/or arc-jet environments which are incapable of achieving complete simulation of actual reentry conditions, i.e., Mach number, Reynolds number, and total enthalpy levels simultaneously. Semi-empirical correlations based on such data must, therefore, be verified through atmospheric flight tests or through short duration freeflight tests within ballistics ranges, wherein actual reentry conditions can be achieved.

5

In recent years, intensive national interest and effort have been focused on the problem of predicting boundary-layer transition onset and location on reentry vehicle nosetips. Numerous systems studies have identified this phenomenon as playing a dominate role in reentry vehicle design considerations, both from a survivability standpoint (e.g., burn-through or thermo-structural failure of the nosetip), as well as from a performance standpoint (e.g., reentry vehicle contributions to overall strategic system accuracy).

Under the PAssive Nosetip Technology (PANT) Program,[1][2] an extensive number of wind-tunnel experiments were conducted and results analyzed in an effort to provide an improved correlation for surface-roughness and wall-temperature effects on nosetip boundary-layer transition.[3] The objective of the present effort was to test the validity of extrapolating this correlation to actual reentry vehicle materials exposed to actual reentry environments.

II   REVIEW OF PANT
TRANSITION CORRELATION

Two series of wind-tunnel tests were conducted at $M_\infty = 5$, $\sim 10^6 \leq Re_\infty/ft \leq \sim 20 \times 10^6$, $\sim .4 \leq (T_w/T_e) \leq \sim .8$, using both polished ($k \approx 0$) and roughened ($0.6 \leq k \leq 80.0$ mils) metal calorimeter models. Uniform surface roughness patterns were created using grit-blasting techniques ($k \leq 3.5$ mils) and copper-particle-brazing techniques ($k \geq 3.0$ mils). Surface roughness dimensions were defined, via optical techniques, as the "distance between the significant peaks and the significant valleys"; supporting profilometer measurements showed such dimensions to be equal to four times the corresponding RMS surface roughness values.[3] Both hemispherical ($0.75 \leq R_N \leq 3.5$ inch) and laminar-blunted ($R_N = 3.5$, 5.0 inch) shapes were tested. Instrumentation consisted of numerous back-face-mounted thermocouples.

[1] Wool, M. R., "Final Summary Report Passive Nosetip Technology (PANT) Program," SAMSO-TR-75-250, Aerotherm/Acurex Corp., Report 75-159, Jun 1975

[2] Various authors, "Interim Reports, Passive Nosetip Technology (PANT) Program," SAMSO-TR-74-86, Vols. I through XXIII, Aerotherm/Acurex Corp., Report 74-100, Apr 1971 through Jun 1975

[3] Anderson, A. D., "Boundary-Layer Transition on Nosetips with Rough Surfaces," Appendix A, SAMSO-TR-74-86, Vol. X, Aerotherm/Acurex Corp., Report 74-100, Jan 1975

Uniform initial temperature models were injected, via a pneumatically driven sting mechanism, into the steady-state supersonic flow. Surface heat-transfer rates were derived from measured temperature-time histories (i.e., the thin-skin calorimeter technique). Transition zone locations were inferred directly from surface heat-transfer distributions.

Transition zone locations, defined in this manner, were noted to move aft as model wall temperature increased. Under certain test conditions, the transition zone moved completely off the nosetip, i.e., initially turbulent temperature-time histories were observed to change slope to values consistent with laminar-flow heat-transfer rates. Such observations of transition "offset" were used to formulate the transition "onset" correlation. Hysterisis effects, if any, associated with relaminarization of an initially turbulent flow are thus embodied in the PANT correlation data base (this subject will be addressed further in the following section).

In its original form, the PANT nosetip boundary-layer transition correlation was expressed as[3]

$$Re_\theta \left[\frac{k}{\theta} \cdot \frac{T_e}{T_w} \right]^{0.7} = \begin{cases} 255, & \text{onset} \\ 215, & \text{location} \end{cases} \qquad (1)$$

Based on theoretical considerations, this correlation was modified to account for mass addition effects, i.e., $B' > 0$; the modified correlation was expressed as[3]

$$Re_\theta \left[\frac{k}{\theta} \cdot \frac{1}{\psi'} \right]^{0.7} = \begin{cases} 255, & \text{onset} \\ 215, & \text{location} \end{cases} \qquad (2)$$

where

$$\psi' = \left[\frac{B'}{10} + \left(1 + \frac{B'}{4} \right) \left(\frac{\rho_e}{\rho_w} \right) \right]$$

In application, a computed value of 255 must be reached or exceeded at the sonic point location; if this condition is satisfied, then the transition zone is predicted to physically begin at the surface point where this parameter attains a value of 215. If predicted to occur, the transition zone will always be located in the subsonic flow region. Figures 2 and 3 schematically illustrate these points.

In the opinion of the present authors, equation (2) well represents the data base on which it was formulated. The theoretical extensions to include mass addition effects were also well formulated. The primary question which must be addressed, however, is whether or not this correlation can be applied with confidence to the design of actual reentry vehicle nosetips, i.e., does it adequately predict transition zone onset/location on ablating carbonaceous nosetips in hypervelocity reentry environments? An experimental program was thus formulated in an attempt to answer this critical question.

III   DEFINITION OF PRESENT EXPERIMENT

The nosetip thermal response and shape change computer code currently utilized at the Naval Surface Weapons Center/White Oak Laboratory was developed under government sponsorship by the Aerotherm/ Acurex Corporation.[4] In its present state, this code has been updated with all aerothermodynamic correlations developed under the PANT program. [1]

In this code, surface roughness effects on both laminar and turbulent heat-transfer rates are modeled by semi-empirical correlations which relate an augmentation factor to some roughness parameter which depends on both surface conditions and smooth-wall flowfield variables. This code was further updated by the present authors with a correlation based on the work of Phinney [5] for surface roughness effects on blunt-body laminar heat-transfer rates. This correlation takes the form

$$K_L = 1 + \left[\frac{\rho_2 V_2 R'_N}{\mu_2}\right]^{\frac{1}{2}} \cdot \left[f\left(\frac{k}{\delta^*}\right)\right] \tag{3}$$

where

$$f\left(\frac{k}{\delta^*}\right) = \begin{cases} .00166 \left(\frac{k}{\delta^*}\right) , & \left(\frac{k}{\delta^*}\right) \leq 2.41 \\ .004 , & \left(\frac{k}{\delta^*}\right) > 2.41 \end{cases}$$

and $\left(\rho_2 V_2\right) = \left(\rho_\infty V_\infty\right)$ by conservation of mass across a normal shock wave. This correlation was assumed to hold at all points on the

---

[4] Rafinejad, D., and Derbidge, T. C., "User's Manual: Sandia Nosetip Analysis Procedure (SNAP)," Aerotherm/Acurex Corp., Report UM-74-57, Dec 1974

[5] Phinney, R. E., "Mechanism for Heat Transfer to a Rough Blunt Body," Letters in Heat and Mass Transfer Journal, Vol. 1, No. 2, 1974, pp 181-186

nosetip where the flow remained laminar, with $\left(\frac{k}{\delta*}\right)$ being evaluated locally. The need for this additional code update, to potentially replace the existing PANT correlation for this phenomenon, became apparent during analyses conducted in References (6) and (7); more conclusive evidence justifying use of the Phinney correlation was supplied by comparing predictions generated by both correlations with present experimental results, as discussed in Section V, A.

In general terms, the required inputs for a calculation are: (a) nosetip environment (e.g., trajectory) and initial geometry; (b) grid networks and initial temperature distributions for internal heat conduction calculations; (c) material thermal properties as functions of temperature; (d) surface roughness characteristics; and (e) ablation thermochemistry model for the material of interest. Given these inputs, computation proceeds according to the flow chart of Figure 4.

Having outlined the PANT nosetip boundary-layer transition correlation and the nosetip thermal response and shape change code wherein it is utilized, attention now focuses on definition of the present experiment.

Figure 5 schematically shows a comparison of PANT transition parameter variations along reentry and ballistics-range trajectories. During reentry, a nosetip has sufficient time exposure, under laminar ablation conditions, to form its characteristic microroughness pattern. As altitude decreases, Reynolds number increases, and nose-tip flowfield conditions capable of amplifying roughness-induced disturbances are eventually achieved, i.e., transition onset occurs.

During a ballistics-range trajectory an initially polished nose-tip would have insufficient exposure time, under conditions of interest, to establish its microroughness pattern; thus, the surface microrough-ness pattern must be formed on the nosetip prior to launch (a tech-nique for meeting this requirement is discussed in Section IV). Further, since the range tube is maintained at a constant static pressure level, a ballistics-range trajectory corresponds to flight at a constant effective altitude, i.e., a horizontal line in the schematic of Figure 5. If high ballistic-coefficient models are employed, then velocity-decay effects can be minimized, i.e., ballistics-range

---

[6] Reda, D. C., Leverance, R. A., and Dorsey, W. G., Jr., "Application of Electro-optical Pyrometry to Reentry Vehicle Nosetip Testing in a Hyperballistics Range," Sixth International Congress on Instrumenta-tion in Aerospace Simulation Facilities, Ottawa, Canada, Sep 1975

[7] Reda, D. C., Leverance, R. A., and Dorsey, W. G., Jr., "Surface Temperature Measurements in Hypersonic Free Flight," Tenth Navy Symposium on Aeroballistics, Fredericksburg, Va., Jul 1975

trajectories of essentially constant Reynolds number can be achieved. Time variation of the PANT transition parameter along a ballistics-range trajectory is thus due primarily to wall temperature effects, the value of this parameter monotonically decreasing as wall temperature increases. Such behavior does not recreate the time history of an actual reentry trajectory, rather it corresponds to time histories experienced during the original wind-tunnel experiments used to formulate the correlation. The critical difference between these ground-based experiments is that the ballistics-range experiment can be conducted using ablating nosetip materials in hypervelocity reentry environments. It must be emphasized again that a transition "offset" experiment was used in the formulation of the PANT correlation, and an "offset" experiment is proposed herein to test the validity of extrapolating this correlation to reentry conditions. Therefore, hysterisis effects, if any, would not be expected to account for any observed discrepancies between predicted transition zone behavior and present experimental results.

Calculations were made, using the computer code and transition correlation described above, in order to define ballistics-range trajectories on which the PANT parameter would cross the critical value of 255. Based on these pre-test predictions, specific trajectories were selected; Figures 6 and 7 and Table 1 summarize post-test predictions for all trajectories actually flown. All tests were conducted utilizing pre-ablated ATJ-S graphite nosetips, with an effective nose radius of 0.43 inch, launched at a nominal velocity of 16,000 ft/sec.

Two points concerning these computations, and their influence on final test matrix selection, should be noted. First, at predicted time of transition offset, values for the parameters (k/θ) and (T_w/T_e), evaluated at the sonic point, were within regimes achieved during the original wind-tunnel experiments, i.e., ~1 and ~0.4, respectively.

Second, tests in both air $(B' > 0)$ and nitrogen $(B' = 0)$ were conducted. Reasons for this were twofold: to ascertain the influence of mass addition on roughness-induced boundary-layer transition and to counter possible arguments that surface recession would change the microroughness during flight. Further elaboration on the subject of surface roughness in flight is called for.

Nosetip models used in the original wind-tunnel experiments were metallic; they experienced no ablation, no recession, and thus each possessed a constant surface roughness throughout its exposure to the test environment. In the present experiment, pre-ablated graphite nosetips experienced turbulent flow conditions upon exposure to the test environment. In air, some minimal amount of surface recession under turbulent flow conditions was predicted to occur. For trajectories on which transition was predicted to leave the nosetip, such surface resession was of the order of three times the median microroughness value, or less (see the last column

10

of Table 1). The question is whether or not such levels of surface recession were sufficient to alter the known initial surface roughness distribution. Should a macroroughness pattern begin to form, it would "fix" transition on the nosetip, and the predicted behavior of transition zone rearward movement with increasing wall temperature would not be observed.

Macroroughness dimensions are typically an order of magnitude greater than microroughness dimensions and currently utilized macroroughness growth models [4] [8] require that a total surface recession equal to five times the macroroughness depth be experienced before this large-scale surface roughness formation is achieved.

It was concluded that predicted levels of surface recession were consistent with the assumption of a constant surface microroughness distribution. Perhaps a more important area of scrutiny lies within the original distribution itself, i.e., is such a distribution (details of which are presented in the next section) best characterized, for transition purposes, by its median value?

Based on these computations, instrumentation was placed such that measurements of nosetip surface temperature contours could be made both uprange and downrange of those stations where transition was predicted to leave the nosetip (see Figure 8). The concept of detecting transition zone presence and location from measurements of nosetip surface temperature distributions was, in fact, defined by these computations. Predicted surface temperature distributions in the presence of a transition zone were noted to possess a definitive change in slope, essentially coincident with the physical beginning of the transition zone. Further, sufficient thermal response time was predicted to exist between measurement stations such that if the transition zone moved off the nosetip, then the occurrence of this event would be observable in measured surface temperature distributions at downrange stations. Details of how these experiments were conducted are presented in Section IV.

IV   AEROTHERMODYNAMIC TESTING TECHNIQUES

The present authors have discussed, in detail, requirements and techniques for conducting aerothermodynamic tests of reentry vehicle nosetips, under controlled reentry conditions, in a hyperballistics range. [9] Four sequential steps were outlined as essential elements for conducting such tests:

---

[8] White, C. A., and Grabow, R. M., "Influence of Scallop Roughness on Nosetip Shape Change Behavior," SAMSO TR 73-88, Jan 1973

[9] Reda, D. C., Leverance, R. A., and Longas, S. A., "Aerothermodynamic Testing and Analyses of Reentry Vehicle Nosetips in Hypersonic Ballistics-Range Flight," 22nd International Instrumentation Symposium, Instrument Society of America, San Diego, CA, May 1976

(1) Select a nosetip material and properly precondition (pre-roughen) it, via material ablation, in an arc-jet environment which most closely simulates the regime of interest, e.g., laminar or turbulent flow.

(2) Characterize, in detail, the post-test surface roughness distribution.

(3) Launch the preconditioned nosetips at hypersonic velocities, utilizing fully enclosed sabots, into well-defined ballistics-range environments.

(4) Measure surface temperature contours on each nosetip at various stations along its ballistics-range trajectory, using electro-optical pyrometer techniques, thereby experimentally defining nosetip transient thermal response.

These points are reviewed separately in following subsections. In actuality, the first three points define requirements for providing known initial conditions concerning nosetip surface roughness and nosetip surface and in-depth temperature distributions, as well as a known flight environment as a function of time. If these requirements are met, then a meaningful comparison between predicted and observed transient thermal response can be made. Such comparisons can thus be utilized to validate nosetip aerothermodynamic correlations under reentry environments.

A. Nosetip Material Preconditioning

Initially polished ATJ-S graphite nosetips, machined from a standard 8-inch-diameter hollow-core billet, were preconditioned within a laminar-flow environment at the Aerotherm/Acurex Corporation Arc Plasma Generator Facility (Mountain View, California). A supersonic anode configuration was combined with a 3.5-inch exit diameter nozzle to produce a test stream with a uniform core of 2.0-inch diameter. Arc-jet test conditions and results are summarized below:

> initial R_N = 0.375"
> test gas = simulated air, 76.8% N_2, 23.2% O_2
> $M_\infty \cong 3.5$
> $P_{STAG} \cong 0.07$ atm
> H_{STAG} (centerline) $\cong 45,000$ Btu/#m
> $T_{SONIC\ POINT}$ (steady-state) $\cong 6,000°R$
> exposure time $\cong 18.5$ sec
> stagnation point recession $\cong .030$ inch
> post-test effective R'_N = 0.43" ($\Psi \angle 45°$)

Such conditions were sufficient to force the entire hemispherical surface to experience ablation in the sublimation regime of graphite.[10]

---

[10]Wakefield, R. M., and Peterson, D. L., "Graphite Ablation in Combined Convective and Radiative Heating," AIAA Journal of Spacecraft and Rockets, Vol. 10, No. 2, Feb 1973, pp 149-154

B. Material Surface Roughness Characterization

Detailed graphite microroughness and material property character-
ization te st s were conducted[11] on two ATJ-S graphite nosetips,
one polished and one preconditioned, wherein established material
characterization techniques[12] were employed. Results pertinent
to the present paper are summarized in Figures 9, 10, and 11.

It should be noted here that the preconditioned nosetip studied
in Reference (11) was found to possess a characteristic microrough-
ness distribution in agreement with previously measured ATJ-S
results.[12] This nosetip, however, represented a first attempt at
preconditioning wherein the microroughness distribution formed only
for $\Psi \leq 30°$ (initial $R_N = 0.50$ inch, test exposure time $\cong 12.0$ sec,
other conditions as previously listed). Based on the recommendations
made in Reference (11), a second attempt at preconditioning was
undertaken (as outlined in the previous subsection); post-test
microscopic examinations of these smaller nose-radius tips revealed
that the combination of reduced nose radius and increased exposure
time was sufficient to achieve the desired surface microroughness
pattern over the entire blunt region of the nosetip.

Of the three distributions shown in Figure 10, the measured
roughness element height distribution is felt to most significantly
influence boundary-layer transition. This distribution was con-
verted to bar-chart format and replotted as Figure 11. This latter
figure most dramatically illustrates that a substantial percentage
of all roughness elements are concentrated in the 5 to 10μ range;
it also illustrates the skewed nature of the distribution, with a
full twenty percent of all roughness elements possessing a measured
height greater than 15.5μ.

Two numerical values were selected from the measured height
distribution for use in present analyses, the median or fifty-per-
centile value (8.9μ) and the twenty-percentile value (15.5μ).
Based on techniques previously applied,[11][12] these measured
values were multiplied by a factor ($4/\pi$) to account for the fact
that the cross-sectional measurement plane (e.g., Figure 9) does
not pass through the exact peaks of the three-dimensional roughness
elements; when applied, the following peak-to-valley roughness
element dimensions resulted:

$$k_{.5} = 0.45 \text{ mils}$$
$$k_{.2} = 0.78 \text{ mils}$$
$$(1\mu = .03937 \text{ mils})$$

---

[11]Dirling, R. B., Jr., "Graphite Microroughness and Material Char-
acterization Tests," McDonnell Douglas Contract Report MDCG-5788,
Apr 1975

[12]Kratsch, K. M., Dirling, R. B., Jr., Johnson, G. P., and Swain,
C. E., "Erosion Mechanisms and Improvement of Graphitic Materials,
Vol II, Hyperthermal Erosion Tests and Surface Roughness Char-
acterization," AFML-TR-70-307, Vol. II, Jun 1972

Preconditioned nosetips were incorporated into flare-stabilized ballistics-range models in such a manner as to preserve this surface microroughness pattern, i.e., all machining, fitting, handling, etc. of the graphite portions of models, in their transition from post-test arc-jet models to pre-test ballistics-range models was accomplished without touching the blunt nosetip region.

C.   Exposure to Controlled Reentry Environments

In order to create valid reentry simulations, hypersonic launch velocities must be achieved. This requirement dictates use of a two-stage light-gas gun. In the present series of tests, a new 4.0-inch I.D. launch tube was mated to an existing 8.0-inch I.D. first-stage (driver) section to achieve muzzle velocities of 16,000 ft/sec. Utilization of this large-scale launch tube enabled 2.0-inch base-diameter models to be launched in fully enclosed sabots (see Figure 12).

This sabot possessed a metallic internal structure and a smooth teflon insert machined to a hemispherical shape. This design served to protect the surface microroughness pattern and overall structural integrity of the nosetip during launch acceleration, as well as to shield the nosetip from heat-transfer effects within an undefined launch tube environment, thereby ensuring a known uniform initial temperature distribution throughout the solid graphite nosetip upon its exposure to the freeflight environment. Stabilizing flares with spiral grooves were incorporated in order to roll the model at a rate ~ 3 revolutions/1,000 feet of flight, thereby minimizing angle of attack and dispersion effects. In addition to these measures, for all shots at $P_\infty \leq 125$mmHg abs. the blast tank was maintained at a pressure level equal to the range-tube pressure, thereby ensuring flight through quiescent environments (i.e., no counterflowing jets).

Through utilization of a quick-opening blast tank valve, the range tube can be independently maintained at any desired static pressure level from atmospheric down to ~ 0.5mmHg abs.; various reentry environments can thus be achieved through appropriate combinations of range tube pressure and launch velocity. Figure 13 shows the maximum operating envelope of this facility in comparison with typical reentry trajectories for slightly blunted sphere/cones; the stagnation pressure and enthalpy corresponding to any point on such a reentry trajectory can be duplicated in hypersonic ballistics-range flight. More specifically, Figure 14 shows free-stream unit Reynolds number, stagnation pressure, and stagnation enthalpy, as functions of freestream velocity for flights through ambient temperature air at various static pressure levels (real gas effects included).

D.   Measurement of Surface Isotherms in Hypersonic Free Flight

Due to severe model launch loads and short test times encountered in ballistics-range research, essentially all data acquisition is accomplished through optical techniques. The present subsection

describes an optical technique for the measurement of surface temperature distributions on freeflight models traveling at hypersonic velocities, electro-optical pyrometry. Details of this system, data reduction procedures, and limiting assumptions in data interpretation, are covered below.

Three electro-optical pyrometer systems were installed along the range tube, with focal planes located at 256, 416, and 576 feet from the muzzle exit. These stations are hereafter referred to as stations 5, 9, and 12 respectively. The physical arrangement utilized in adapting this system to the present facility is shown schematically in Figure 15. The basic operating principle of such electro-optical pyrometers is to record, on film, images of known temperature sources and the image of an unknown temperature source; application of the resulting calibration relationship between source brightness temperature and film density allows temperature distributions on the unknown temperature source to be determined.

To obtain the required calibration of film density versus source temperature, a specially designed carbon arc is incorporated (Mole-Richardson Co., Hollywood, California). Electrodes of this unit are positioned to yield a 120-degree included angle between them, thereby allowing end-on observations of the positive graphite electrode via proper alignment of the planar mirror in the range tube. The crater of the positive electrode, when operated under properly chosen voltage and current conditions, provides a source of high temperature radiation of exceptionally high reproducibility (3806° $+10^{\circ}$K). A series of calibration filters (traceable to the National Bureau of Standards) allows effective blackbody temperatures from $\sim2200^{\circ}$K to $\sim3800^{\circ}$K to be generated; effective temperatures above 3800°K are achievable by photographing the unfiltered image at larger camera lens apertures than are used for recording actual freeflight data.

At the receiving end of the optical path is an image converter camera; two types are currently utilized. Cameras at stations 9 and 12 consist of a planar photocathode, a planar phosphor screen, a relay lens, and a sliding film back (4" x 5" negatives). The unit at station 5 has a fixed film plate in direct contact with the phosphor screen, i.e., no relay lens. This latter arrangement (which requires the camera itself to be mounted on a traversable platform) yields markedly increased sensitivity versus the more conventional units (i.e., seeable temperatures down to $\sim2100^{\circ}$K versus $\sim2600^{\circ}$K for the other two units).

When a high voltage pulse is applied across the photocathode/phosphor screen region, any light image incident on the photocathode surface is transferred, via accelerated electrons, to the phosphor screen; the recreated light image is then relayed or directly transferred to the exposed film surface and recorded. Since electron image propagation is effectively maintained only in the presence of a high voltage acceleration field, an effective electronic shutter time can be set by preselecting the time duration

of the voltage pulse. Exposure times of the order of 0.1 to 1.0 microseconds can thereby be attained, minimizing motion blur.

Figure 16 shows component and overall system response as a function of incident light wavelength. Use of a cut-off filter, $W_{12}(\lambda)$, coupled with the photocathode tube responses of $S_{20}(\lambda)$ at station 5 and $S_{11}(\lambda)$ at stations 9 and 12, serves to limit monitored wavelengths to the ranges $0.50 \leq \lambda \leq 0.85$ micron at station 5 and $0.50 \leq \lambda \leq 0.65$ micron at stations 9 and 12. By monitoring such narrow wavelength bands, overall system performance is improved in two areas: first, within this wavelength regime, the calibration source exhibits true blackbody characteristics, and second, contributions to the data signal from gas cap radiation are greatly reduced. (Calculation of and correction for the gas cap contribution are discussed under limiting assumptions later in this subsection).

One problem encountered during calibration, but not during actual data recording, concerns the small but finite bleed-through of light transmitted by the image converter tube. During free-flight observations, the model image is rapidly swept through the prescribed field of view due to its high velocity, thereby serving to limit the total amount of light received at the photocathode surface. Since the calibration arc is stationary, its long duration signal would, despite the short absolute shutter time of the image converter camera, result in noticeable bleed-through of light, thus fogging the film. This is countered by sweeping the arc image across the photocathode field of view by means of a rotating mirror while limiting the impingement on the tube surface to a single pass via a light detector/electronic delay circuit/mechanical shutter arrangement.

All calibration images are recorded on a single negative via the sliding film back or traversable camera arrangement. At the completion of calibration, the planar mirror is rotated (onto an identical optical path) to view the approaching flight path; all final optical alignments are accomplished with a CW laser. Standard test procedures are then initiated, culminating with model launch and data acquisition. The nosetip brightness image is always recorded on the same negative used for calibration in order to eliminate film development inconsistencies.

The 4" x 5" film sheet, containing all calibration images plus the model image, is developed (Figure 17 shows a positive print of one such negative). Calibration images on the resulting negative are scanned with a microdensitometer and film density levels are simultaneously plotted by an isodensitracer (see Figure 18). In this procedure, all film densities are measured relative to a reference density level generated by scanning a separate piece of high quality uniform density film (referred to here as the reference filter). Use of a reference filter is dictated by possible requirements for shifting the isodensitracer scale

limits higher or lower in order to accommodate nosetip image density levels within available plotting space; a rescan of this reference filter under any new density scale constraints supplies a repeatable reference level from which nosetip image density levels may be measured. An example of a pyrometer calibration curve generated in this manner is shown in Figure 19.

Figure 20 shows two end-on images of pre-ablated ATJ-S graphite nosetips as they appeared on developed data negatives. These images were recorded by the same image-converter camera after identical times-of-flight through air. The upper negative was recorded for flight through a P_∞ = 100mmHg abs. environment and is typical of all such images recorded under transitional flow conditions, i.e., conditions under which the transition zone, as inferred from measured surface temperature distributions, had its origins away from the stagnation point. A finite region of relatively constant film density was observed, surrounded by an essentially concentric band of dark (hot) spots, the spots themselves being distributed randomly within the band. The lower negative was recorded for flight through a P_∞ = 200mmHg abs. environment. Under these conditions, a local minimum in film density was observed at the stagnation point, followed by an immediate rise to peak densities away from the stagnation point. Here the film density distribution was observed to be very concentric and void of the randomly distributed hot spots discussed above.

All such nosetip images are scanned by the microdensitometer and resulting film density levels plotted by the isodensitracer. Two distinct types of plots are generated (see Figure 21). First, a complete scan of the entire nosetip image is made and color-coded isodensity contours of this end-on view are simultaneously plotted by the isodensitracer. After the overall scan is complete, selected cross-cut planes are rescanned and relative film density is plotted as a function of physical location (such cross cuts are usually taken on a major diameter, through the geometric stagnation point). These analog plots of relative film density versus physical displacement along a major diameter can be digitized through use of appropriate scale factors. Results can thus be replotted as nosetip surface temperature versus non-dimensional arc length (S/R_N) along the nosetip surface.

Strictly speaking, the pyrometer calibration procedure relates relative film density to source brightness temperature. In order to equate brightness temperatures measured by the electro-optical pyrometer system to model surface temperatures certain limiting assumptions must be invoked. These are discussed next.

First, it is required that, within the monitored wavelength regime, surfaces under observation radiate incandescently according to Planck's equation, i.e., radiate with black-or grey-body characteristics. This assumption is justifiable for bulk graphites and carbonaceous ablation chars (i.e., nosetip materials of current interest) which possess smooth, near unity, emissivity-versus-

temperature curves throughout the visible spectrum.[13] For such materials, the system calibration procedure is most valid since both the calibration arc electrode and the nosetip are carbonaceous and both radiate as black or near-black body sources.

Second, ablation phenomena at or near the model surface must not measurably influence recorded brightness images. Surface thermochemistry is a function of nosetip material and the gaseous environment to which it is exposed. Violent chemical reactions (e.g., combustion), which can occur at various metallic surfaces exposed to high-temperature oxidizing environments, and melt layers, which can occur on certain ablating surfaces (e.g., quartz phenolic), would most likely attenuate, i.e., add to or detract from, surface radiation. However, subliming and/or charring carbonaceous ablators, which yield gaseous products of ablation, are felt to meet this second restriction.

Third, it must be assumed that the flow field itself does not attenuate the surface radiation signal. At hypersonic velocities, a strong bow shock wave forms ahead of the blunt nosetip. Between this bow wave and the model surface there exists a thin, dense, real-gas shock layer. This region, referred to here as the gas cap, contains, depending on flight conditions and range tube gas, various dissociated and/or ionized species. Effects of both gas cap absorption and emission on the surface radiation signal must be ascertained.

Gas cap absorption effects can be neglected if the product of absorption coefficient times local shock layer thickness is small compared to unity. Based on reported absorption coefficients for air at maximum density and temperature conditions experienced under present test conditions[14], this product was computed to be of the order of 10^{-2}.

Figure 22, also based on Reference (14) shows the energy radiated into spherical space by a unit volume of air at temperature and density conditions bracketing most ballistics-range environments of interest as a function of wavelength. If at any point on the nosetip one calculates the local shock wave stand-off distance

---

[13] Wilson, R. G., and Spitzer, C. R., "Visible and Near-Infrared Emittance of Ablation Chars and Carbon," AIAA Journal, Vol. 6, No. 4, Apr 1968, pp 665-671

[14] Gilmore, F. R., "Approximate Radiation Properties of Air Between 2000° and 8000°K," Rand Corp. Memo RM-3997-ARPA, Mar 1964

(i.e., the local depth of radiating gas) and subsequently computes the integral listed at the bottom of Figure 22, a measure of the local gas cap radiation (energy/unit area) can be derived. In this calculation, the one-half factor accounts for that portion of the radiant energy per unit volume directed towards the sensing instrument. A computer code for performing the above calculations was developed in Reference (15) and has been applied here.

Having calculated the energy per unit area radiated by the gas cap to the image converter camera, it remains to devise a procedure whereby corrections for this contribution to the data signal can be made. A relationship between energy per unit area sensed by the pyrometer and brightness temperature of the radiating source is thus required.

Figure 23 shows the energy radiated into hemispherical space by a unit area of a black ($\varepsilon = 1$) and a grey ($\varepsilon = .9$) surface, each at 7000°R, as a function of wavelength. Photocathode tube response ($S_{11}(\lambda)$) and overall pyrometer system response ($S_{11}(\lambda) \cdot W_{12}(\lambda)$) to the grey-body energy input are also shown. An integration with respect to wavelength of this lower curve yields the energy per unit area sensed by the electro-optical pyrometer system for a grey body at the specified surface temperature. Such calculations were made for both black and grey ($\varepsilon = 0.9$) surfaces over the full operating temperature range of the present pyrometer systems (both $S_{11}(\lambda)$ and $S_{20}(\lambda)$ tubes) and results are shown in Figure 24. Several points concerning this figure should be made.

First, an uncertainty in surface emissivity of the order of ten percent results in only a 30-50°K uncertainty in surface brightness temperature. Second, an equivalent blackbody brightness temperature can be defined for any computed gas cap radiation level. Third, corrections to measured surface temperatures for gas cap radiation can be made as noted below. For any specified position on the nose-tip, Figure 24 defines a radiant energy level corresponding to the measured brightness temperature. An independent calculation of local gas cap radiant energy per unit area is made, and this value is subtracted from the experimentally defined energy level. The resulting net energy level is attributed to surface radiation, and a corrected model surface temperature is thus defined.

Under conditions of the present experiment, gas-cap corrections were found to be everywhere less than $|-100°R|$, and as such, were not applied.

15

Miller, J. T., Unclassified Appendix to "Development of an Aeroballistics Range Testing Capability for Blunt Body Boundary-Layer Transition Studies," AEDC-TR-73-117, Jul 1973 (Conf)

V   EXPERIMENTAL RESULTS VS PREDICTIONS

During the present program, a total of eight data shots were made, five in air and three in nitrogen. Nosetip images recorded during these tests were scanned and plotted according to techniques described in Section IV, D. Surface temperature distributions so obtained are presented herein as T vs (S/R_N) plots on two rays, 180° apart. Results presented in this manner give a representative indication of circumferential data spread noted for each case.

This section is subdivided into three subsections. The first summarizes results concerning roughness effects on laminar heat-transfer rates; the second and third subsections present and discuss results for flights through air (B'> 0) and nitrogen (B' = 0), respectively.

A.   Roughness Effects on Laminar Heat-Transfer Rates

As discussed in Section III, specific test conditions and instrumentation locations for the present experiment were selected based on pre-test calculations of nosetip transient thermal response. Since the nosetip boundary-layer transition correlation in question possesses a strong wall-temperature dependence, predicted flight times to transition offset are obviously dependent on methods used to calculate surface heat-transfer rates. Results of the present experiment substantiated use of equation (3) to model roughness effects on laminar heat-transfer rates.

Figure 25 summarizes these results by comparing stagnation point temperatures, predicted via the PANT[1] and Phinney[5] correlations, with measured values. All data shown in Figure 25 were obtained under conditions which resulted in the presence of a transition zone within the subsonic flow region of the nosetip.

The PANT correlation predicted no augmentation (K_L = 1.0) under present test conditions; stagnation point temperatures so predicted were consistently 30 to 50 percent below measured values. Phinney's correlation predicted augmentation factors of ~1.8 $\leq K_L \leq$ ~2.3; stagnation point temperatures so predicted were within ±10% for 10 of the 14 data points shown, and within ±12-1/2% for 12 of these same 14 measured values.

B.   Flights Through Air

Flights were conducted through air at freestream static pressure levels .112 $\leq P_\infty \leq$ .263 atm. (~30 $\leq P_{STAG} \leq$ ~70 atm.), i.e., under conditions ranging from predicted transition offset prior to the first data monitoring station, to conditions under which a transition zone was predicted to exist on the nosetip throughout the entire monitored portion of its flight (recall Table 1).

20

Aerothermodynamic trajectories for all these flights, and comparisons of predicted and measured surface temperature distributions, are shown in Figures 26 through 39.

At low freestream static pressure levels (P_∞ = 85 and 100mmHg abs.), measured distributions were found to possess a region of essentially constant temperature, followed by a definitive change in slope, resulting in peak surface temperatures away from the stagnation point. The extent of this constant temperature region was observed to decrease as the freestream static pressure level was increased; at a static pressure level of 200mmHg abs. this region of constant surface temperature was eliminated entirely, the beginning of the temperature rise becoming coincident with the stagnation point itself. Further, for a given static pressure level ($85 \le P_\infty \le 125$mmHg abs.) the extent of this constant temperature region was observed to decrease slightly with flight time, i.e., with increasing surface temperature level.

As suggested by pre-test calculations, both the presence and location of a transition zone were clearly evident through observations of nosetip brightness images and resulting measured surface temperature distributions.

Repeatability of such measured distributions was found to be reasonable based on two attempts, one in air and one in nitrogen. Figures 33 through 35 illustrate the case for air, wherein measured surface temperature levels were noted to be of the order of 500^OR in variance, out of an absolute temperature level of the order of 5000^OR, or approximately a 10% data spread between the two flights. Such differences were of the same order as circumferential variations in surface temperature observed within the transition zone region for any single flight, due to the presence of localized hot spots.

Since all requirements for the aerothermodynamic testing of nosetips in a hyperballistics range (as previously discussed) were adhered to in the present tests, all inputs and initial conditions required for conducting transient thermal response analyses were known. A constant surface roughness of 0.45 mil (median value) was used for the computation of roughness-augmented heat-transfer rates in both laminar and turbulent flow regions. Also, as discussed previously, two microroughness dimensions were utilized with the PANT correlation for predictions of boundary-layer transition onset and location, $k_{.5}$ = 0.45 mil and $k_{.2}$ = 0.78 mil.

As noted in the T vs (S/R_N) plots under discussion, at least three and, in all but the lowest P_∞ case, four predicted surface temperature distributions are shown. Differences between these predicted distributions themselves are a direct result of techniques used to model roughness augmentation of laminar heat-transfer rates and transition zone presence/location. All other code inputs and options were identical.

A review of the four predicted distributions found in Figure 29 serves to describe these differences. The bottom, or lowest temperature level, distribution resulted from use of the code's original (PANT) correlations[1] for these two phenomena. The middle two distributions resulted from use of Phinney's correlation[5] for roughness effects on laminar heat-transfer rates, coupled with the PANT transition correlation (equation (2)), utilized with $k = k_{.5}$ and k_2, respectively. The uppermost distribution resulted from use of an all-turbulent-flow option (boundary-layer transition mathematically fixed at the first computation point away from the stagnation point); here, Phinney's correlation was applied solely at the stagnation point. In all cases, a finite length transition zone model[4] and the PANT correlation for roughness effects on turbulent heat-transfer rates[1][4] were utilized.

Predicted levels of surface temperature were found to be in good agreement with measured levels once roughness effects on both laminar and turbulent heat-transfer rates were accounted for. Predicted shapes of surface temperature distributions were strongly dependent on predicted transition zone presence and location. Experimental results clearly show that the transition zone did not move off the nosetip as predicted by the PANT correlation utilizing the median microroughness dimension of 0.45 mil (see, for example, the time sequence of predictions in Figures 29, 30, and 31).

Figures 40 through 42 summarize predicted and experimentally inferred transition zone locations, plotted as functions of free-stream static pressure level, for each of the three data monitoring times. Results are shown in these coordinates since $(S/R_N)_{TR}$, P_∞, and t are directly measurable quantities, independent of any calculations.

Transition zone locations, as inferred from measured surface temperature distributions, were noted to progress forward, towards the stagnation point, as the freestream static pressure level was increased (i.e., as flight Reynolds number was increased). Experimentally defined transition zone locations were also noted to progress slightly forward, for a constant P_∞ level, as wall temperature increased.

This latter observation was not a result of lateral conduction effects. Calculations were made for shot 2003 wherein transition was mathematically fixed at $(S/R_N) = .287$ for all times (see Figure 43). Predicted surface temperature distributions clearly showed that the change in slope remained coincident with the start of the transition zone. Such predicted behavior was consistent with that noted for calculations made utilizing the PANT transition correlation, the change in slope remaining essentially coincident with the wall-temperature (time) dependent transition zone location.

Predicted transition zone locations, plotted as solid symbols in Figures 40 through 42, are for the actual trajectories flown. Transition offset pressure levels at each of the three data monitoring times, for the 0.45 mil case, were defined from pre-test calculations presented in Figure 7.

At pressure levels (Reynolds numbers) of the present experiment, for k = 0.78 mil, transition offset was not predicted to occur.

Comparisons of predicted and experimentally inferred transition zone locations, for flights through air, led to the following observations.

First, utilization of $k = k_2 = 0.78$ mil with the PANT correlation resulted in predicted transition zone presence, and locations, more nearly in agreement with experimental results, as compared to predictions generated using the median microroughness, 0.45 mil. This fact is somewhat consistent with the definition of surface roughness, k, as measured on the original calorimeter models, i.e., "the distance between significant peaks and significant valleys". Characterization of an ablated surface microroughness distribution by its median value, for transition purposes, may be unjustifiable.

For increasing Reynolds number, present experimental results showed a more rapid approach of the transition zone to the immediate vicinity of the stagnation point, versus the PANT correlation. (Recall levels of agreement between all-turbulent-flow predictions and measured surface temperature distributions for the highest Reynolds number trajectory flown, as presented in Figures 37 through 39.) This fact, coupled with present results concerning roughness-augmentation in laminar-flow regions, have strong implications for shape-change occurring on actual reentry trajectories. One direct result would be a more rapid formation of self-similar, turbulent/biconic shapes, and a reduced probability for the formation of highly irregular or "proboscidean" shapes.[1]

Finally, transition zone aft movement with increasing wall temperature, observed during the original PANT wind-tunnel experiments (B' = 0), was not observed herein for pre-ablated graphite nosetips exposed to reentry conditions (B' > 0).

C. Flights Through Nitrogen

A total of three data flights were conducted in nitrogen, all at $P_\infty = 125$ mmHg abs. ($P_{STAG} \cong 40$ atm.); Figure 44 shows the aero-thermodynamic trajectory. Under these conditions, the PANT correlation, utilized for $k = k_5$, predicted that the transition zone would move off the nosetip at t = .029 sec. Tests in nitrogen were conducted for two reasons, as noted earlier: first, no ablation occurred (B' = 0), and second, because of this fact, the initial surface microroughness distribution remained unaltered

throughout the flight. These two features resulted in ballistics-range tests which most closely simulated the original wind-tunnel tests used to obtain the PANT correlation data base, i.e., an initially uniform temperature model, of specified and constant surface roughness, exposed to a test "stream" wherein the only influence of the "flow" was to aerodynamically heat the surface.

Shot #2001 was the first such test conducted. Results obtained during this flight are shown at the top of Figure 45 and in Figure 46. This single nosetip brightness image (recorded with the most sensitive image-converter camera) clearly indicated the presence of a transition zone at t = .016 sec. Only a few isolated hot spots ($\approx 4800^{\circ}R$) were observed on the data negative recorded at station 9 (t = .027 sec.); no "seeable" image was recorded at station 12 (t = .037 sec.).

No conclusions concerning transition offset could be reached from this initial test. Figure 46 does show, however, that surface temperature levels were well predicted (as was the case in air) once surface roughness effects on both laminar and turbulent heat-transfer rates were correctly modeled. Transition zone location was more realistically predicted by the PANT correlation utilizing $k = k_{.2} = 0.78$ mil, as opposed to that predicted for $k = k_{.5} = 0.45$ mil.

Following completion of all flights through air, the most sensitive pyrometer system was relocated from station 5 to station 12 and two additional nitrogen tests, duplicating #2001, were conducted. Data acquisition was limited to this single station, at t = .037 sec.; results are shown at the bottom of Figure 45 and in Figure 47.

Nosetip brightness images recorded during these two flights were essentially identical, and unlike any others previously observed. These images were void of localized hot spots and other steep gradients in film density. Resulting surface temperature distributions were coincident with one another, remaining essentially constant, at $\sim 4250^{\circ}R$, for $0 \leq S/R_N \leq \sim.5$, thereafter gradually decreasing to below seeable limits downstream of the sonic point.

One could infer from these experimental results that the transition zone had, in fact, moved aft, off the nosetip somewhere between t $\cong$ .027 sec. and t = .037 sec.

Two questions concerning obvious inconsistencies with previous observations and predictions were then raised. First, why did the PANT transition correlation, utilizing $k = k_{.2} = 0.78$ mil. reasonably predict the transition zone location at t = .016 sec., while, in order to achieve a prediction of transition offset, a value of $k = k_{.5} = 0.45$ mil had to be utilized?

Second, why were observed levels of surface temperature at t = .037 sec. well below values predicted by utilization of Phinney's correlation (~5400°R at the stagnation point; predicted distribution not shown in Figure 47)?

Measured transition zone locations, for flights through both air and nitrogen, were consistently at, or upstream of, locations predicted by the PANT correlation utilizing $k = k_{.2} = 0.78$ mil. Obviously, these same measured positions were even further upstream from locations predicted by the PANT correlation using the median microroughness dimension, 0.45 mil. Given these facts, it becomes difficult to explain a correct prediction of transition offset, utilizing the median microroughness dimension, for flights through nitrogen. In order to correlate the entire PANT wind-tunnel data base, a two part transition criterion had to be established, one for transition onset and one for transition zone location. Use of two distinct surface roughness values, one for each part of this correlation, hardly seems justifiable. No answer to the present contradiction is offered here; it may well rest with whatever mechanism(s) created the apparent need for a two part correlation.

The second question was addressed and a plausible explanation offered by the prediction described in Figure 47. Phinney's correlation for roughness effects on laminar heating was applied, in conjunction with the PANT transition correlation for $k = k_{.5} = 0.45$ mil. resulting in the predicted surface temperature distribution at transition offset (t = .029 sec.) shown in Figure 47. At transition offset, application of Phinney's correlation was terminated, and smooth-wall laminar heat-transfer rates were applied (t > .029 sec.). Surface temperatures predicted to exist on the nosetip at transition offset were considerably above levels which could be maintained by these reduced heat-transfer rates. A relaxation of the temperature distribution was predicted to occur, until levels consistent with smooth-wall heat-transfer rates were attained. At t = .037 sec., the predicted distribution closely matched the data.

The apparent success of this analysis suggests a possible underlying mechanism for the phenomenon of roughness augmentation of laminar-flow heat-transfer rates. For nosetip flights through quiescent environments, achieving augmentation factors, K_L, of the order of two may be predominantly dependent on the presence of a transition zone in the subsonic flow region. In other words, the dominant role of surface roughness is to cause boundary-layer transition, which in turn, due to its unsteady nature, propagates disturbances throughout the subsonic shock layer, creating an

effective freestream turbulence level. In actuality, the
formulation of Phinney's correlation represented an extension
of Reference (16), wherein freestream turbulence itself was
noted to be the mechanism for augmentation of stagnation-point
heat-transfer rates in incompressible flow. More work in this
area is required before a complete understanding can be achieved.

VI. SUMMARY AND CONCLUSIONS

An experimental program was conducted to test the validity of
extrapolating the PANT nosetip boundary-layer transition correlation
to actual nosetip materials, in exposure to actual reentry environ-
ments. Pre-ablated ATJ-S graphite nosetips were launched at hyper-
sonic velocities, utilizing fully enclosed sabots, on specific
ballistics-range trajectories through both air and nitrogen. Nose-
tip surface temperature contours were measured via electro-optical
pyrometry, from which transition zone presence and location were
inferred. Based on these measured surface temperature distributions,
and their comparisons with predictions generated via existing PANT
technology, the following observations were made:

1. Measured transition zone locations, for flights through both
air and nitrogen, were found to be considerably upstream of locations
predicted via the PANT correlation utilizing the median surface
microroughness value of ATJ-S graphite, $k_{.5} = 0.45$ mil. Utilization
of the twentieth-percentile value of the ATJ-S microroughness
distribution, $k_{.2} = 0.78$ mil, resulted in more realistic predictions
of transition zone locations, primarily at the lower Reynolds
number/early flight time conditions. For increasing Reynolds
number, present experimental results (in air) showed a rapid
approach of the transition zone to the immediate vicinity of the
stagnation point, as compared to behavior predicted by the PANT
correlation utilizing either k value.

2. For flights through air ($B' > 0$), transition zone aft move-
ment with increasing wall temperature was not observed to occur,
as predicted via the PANT correlation. In contrast, experimentally
inferred transition zone locations were observed to move forward
slightly with increasing wall temperature, i.e., with increasing
time of flight. Predictions of transition zone offset with
increasing wall temperature, generated for $k = k_{.5} = 0.45$ mil,
were thus not substantiated by present results.

Conclusions (1) and (2) concerning flights in air, were most
pertinent to the question at hand: extrapolation of the PANT
transition correlation to reentry materials in reentry environ-
ments. Significant discrepancies between predicted and experimentally
observed transition zone behavior were encountered.

---

[16]Galloway, T. R., "Enhancement of Stagnation Flow Heat and Mass
Transfer Through Interactions of Freestream Turbulence," Journal
of American Institute of Chemical Engineering, Vol. 19, No. 3, May
1973, pp 608-617

3. For flights through nitrogen (B' = 0), transition zone offset with increasing wall temperature was concluded to have occurred, as predicted by the PANT correlation for $k = k_5 = 0.45$ mil. This fact was in contradiction with conclusion (1) concerning use of k_2 for better approximation of transition zone locations. Flights in nitrogen, however, more closely resembled original wind-tunnel tests used to generate the PANT correlation data base, and, for this reason, were less pertinent to the question at hand.

4. Significant effects of surface roughness on laminar-flow heat-transfer rates were observed under present test conditions, for flights through both air and nitrogen, contrary to predictions generated with the existing PANT correlation for this phenomenon. Utilization of a correlation based on the work of Phinney[5] resulted in predicted surface temperature levels in good agreement with measured values. Experimental results obtained during flights through nitrogen (where transition offset was observed), indicated a dependence of this phenomenon on the existence of a transition zone in the subsonic flow region of the nosetip.

TABLE 1   SUMMARY OF TEST CONDITIONS

SUMMARY OF TEST CONDITIONS*

SHOT #	P_∞ (mm Hg, abs)	PREDICTED t (SEC) FOR TRANSITION OFFSET	M_∞	Re_∞/ft.	P_{STAG} (atm)	T_{STAG} (°R)	H_{STAG} (BTU/#m)	$Re_{\theta, SONIC}$	$\left(\frac{k}{\theta}\right)_{SONIC}$	$\left(\frac{T_w}{T_e}\right)_{SONIC}$	$\left(\frac{\rho_e}{\rho_w}\right)_{SONIC}$	B'_{SONIC}	Δr_{SONIC} (mils)
2004	85	0.013	14.36	1.18×10^7	30.78	10,991	5135	105.6	1.10	0.335	0.284	0.175	0.71
2003	100	0.017	14.17	1.36×10^7	35.24	10,907	5036	110.9	1.22	0.405	0.344	0.175	0.88
1999, 2002	125	0.023 0.024	13.92	1.61×10^7	42.48	10,724	4832	117.6	1.39	0.510	0.438	0.175	1.43
2001 2010, 2013	125 (N₂)	0.029	13.48	1.61×10^7	39.54	12,496	4795	111.3	1.24	0.412	0.389	0	0
2000	200	> 0.049 ≠	13.43	2.52×10^7	63.24	10,510	4599	137.2	1.82	0.703	0.633	0.199	3.05

*ALL NUMERICAL VALUES CALCULATED AT PREDICTED TIME OF TRANSITION OFFSET; $K_L > 1$, AFTER PHINNEY, PLUS PANT TRANSITION CORRELATION WITH k = 0.45 mil UTILIZED.

≠ VALUES CALCULATED AT FINAL DATA MONITORING STATION, 0.037 SEC.

28
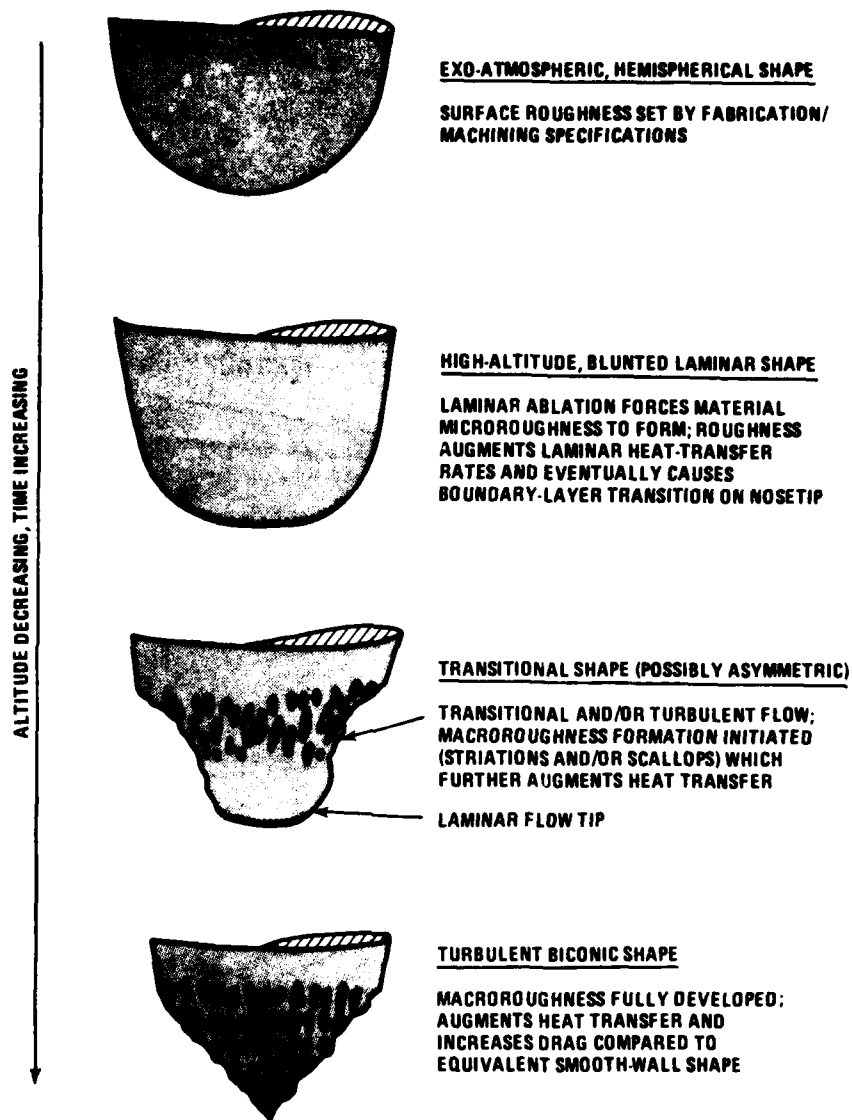
FIG. 1 SCHEMATIC OF NOSETIP SHAPE CHANGE DURING REENTRY
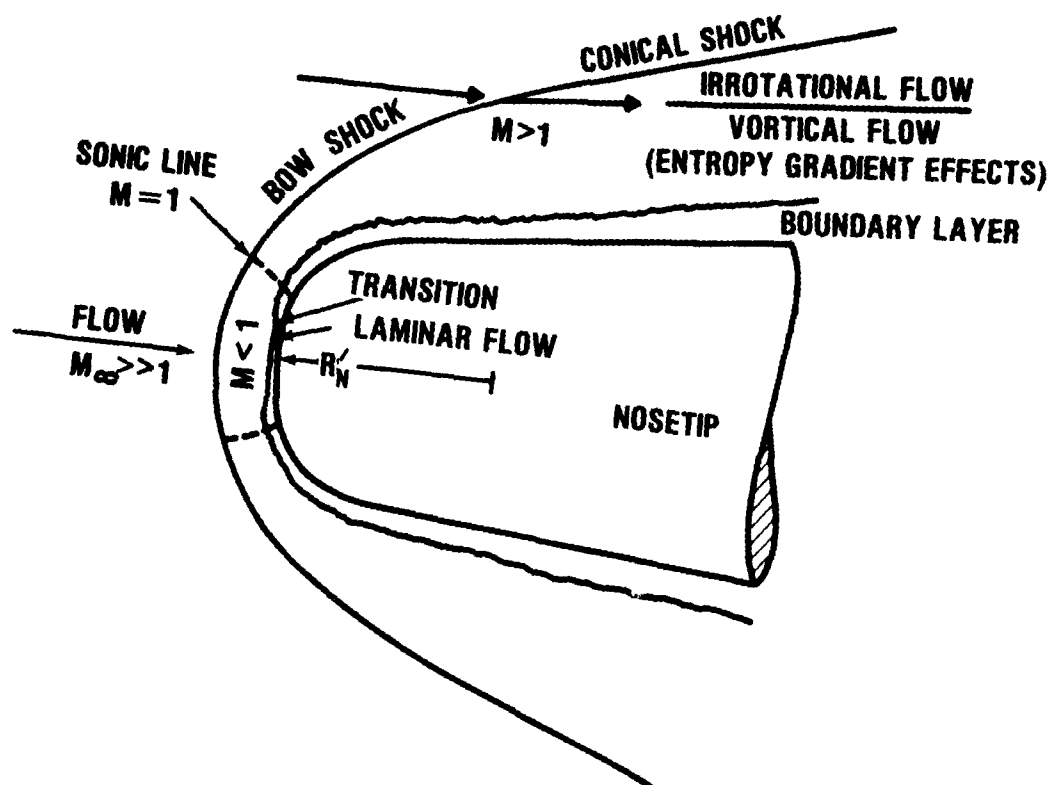
FIG. 2   NOSETIP FLOWFIELD SCHEMATIC AT TRANSITION ONSET
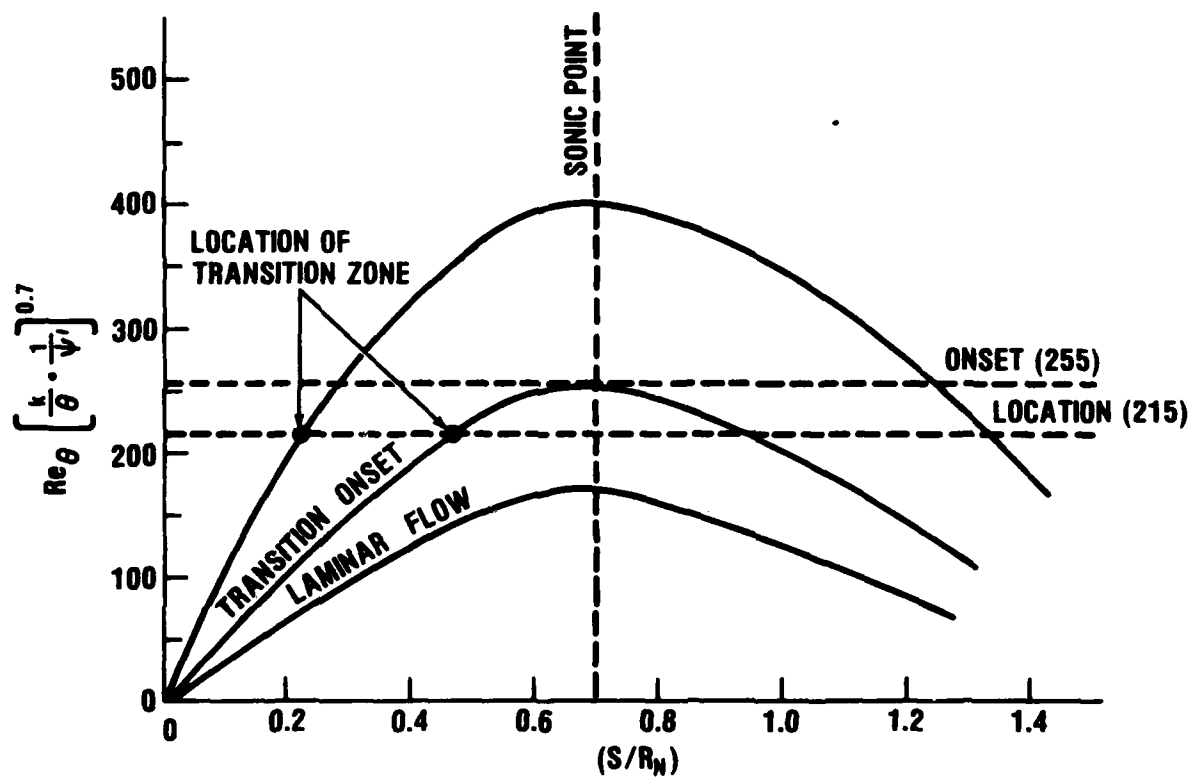
FIG. 3   SCHEMATIC OF PANT TRANSITION PARAMETER vs. (S/R_n)
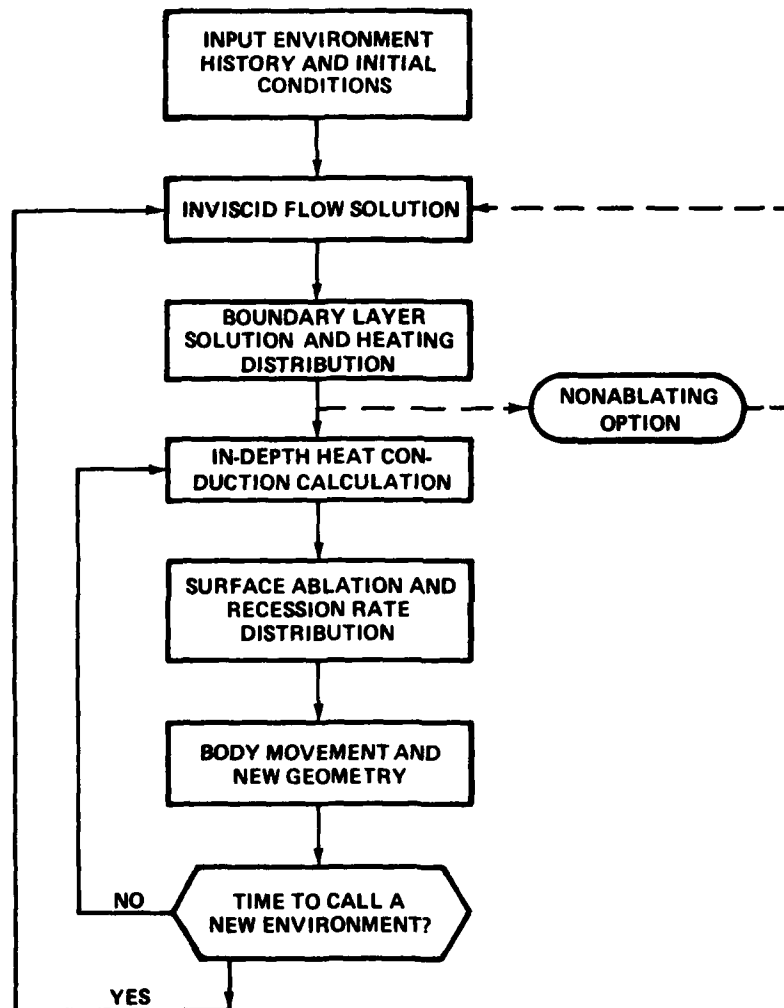
FIG. 4 NOSETIP THERMAL RESPONSE AND SHAPE CHANGE PROCEDURE
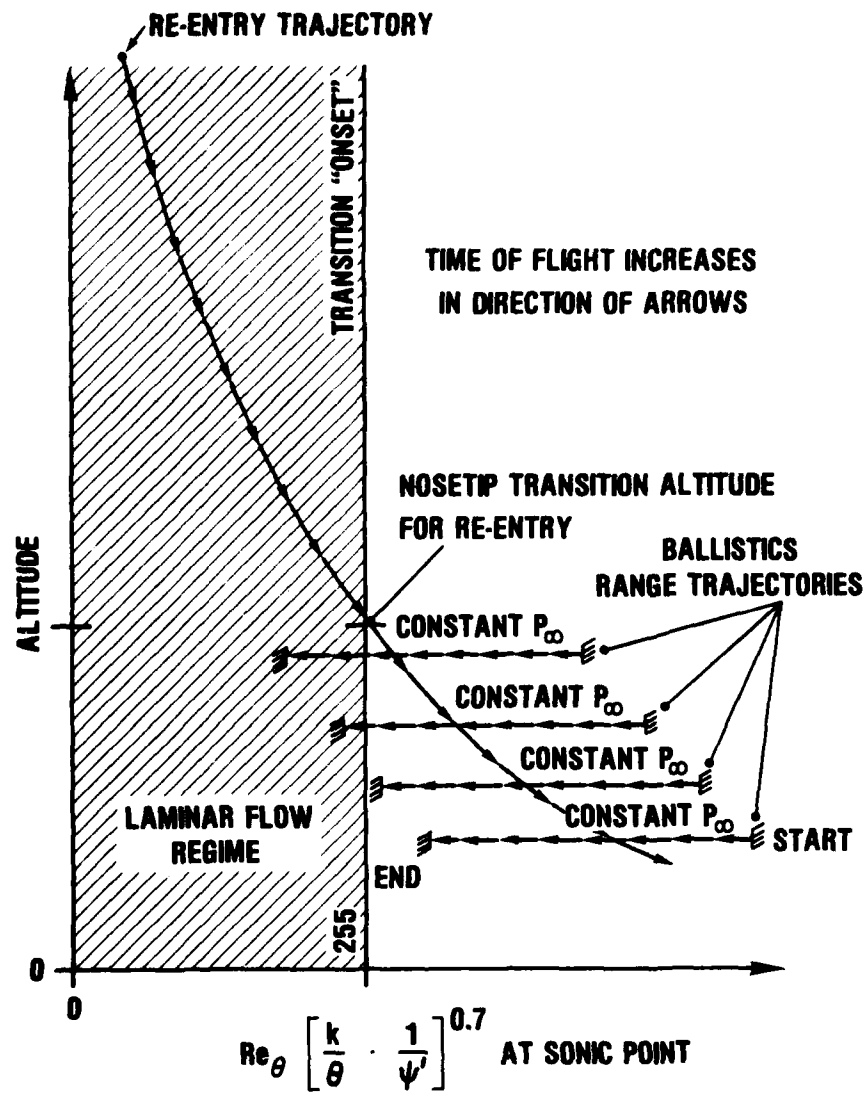
FIG. 5 PANT TRANSITION PARAMETER HISTORIES FOR REENTRY AND BALLISTICS RANGE TRAJECTORIES

SNAP CODE PREDICTIONS FOR
BALLISTICS-RANGE TRAJECTORIES

$K_L > 1$, PHINNEY, UTILIZED

$k = k_{.5} = 0.00045"$, PRECONDITIONED ATJ-S

$R'_N = 0.43"$

$V_i \cong 16,000$ FT/SEC

$T_\infty \cong 530$ °R, AIR, EXCEPT AS NOTED

● TIME AT WHICH TRANSITION IS
  PREDICTED TO LEAVE NOSETIP (PANT)

LAMINAR FLOW REGIME

SHOT:	2004	2003	1999,2002	2001	2000
P_∞ : (mmHg)	85	100	125	125	200 (N_2)
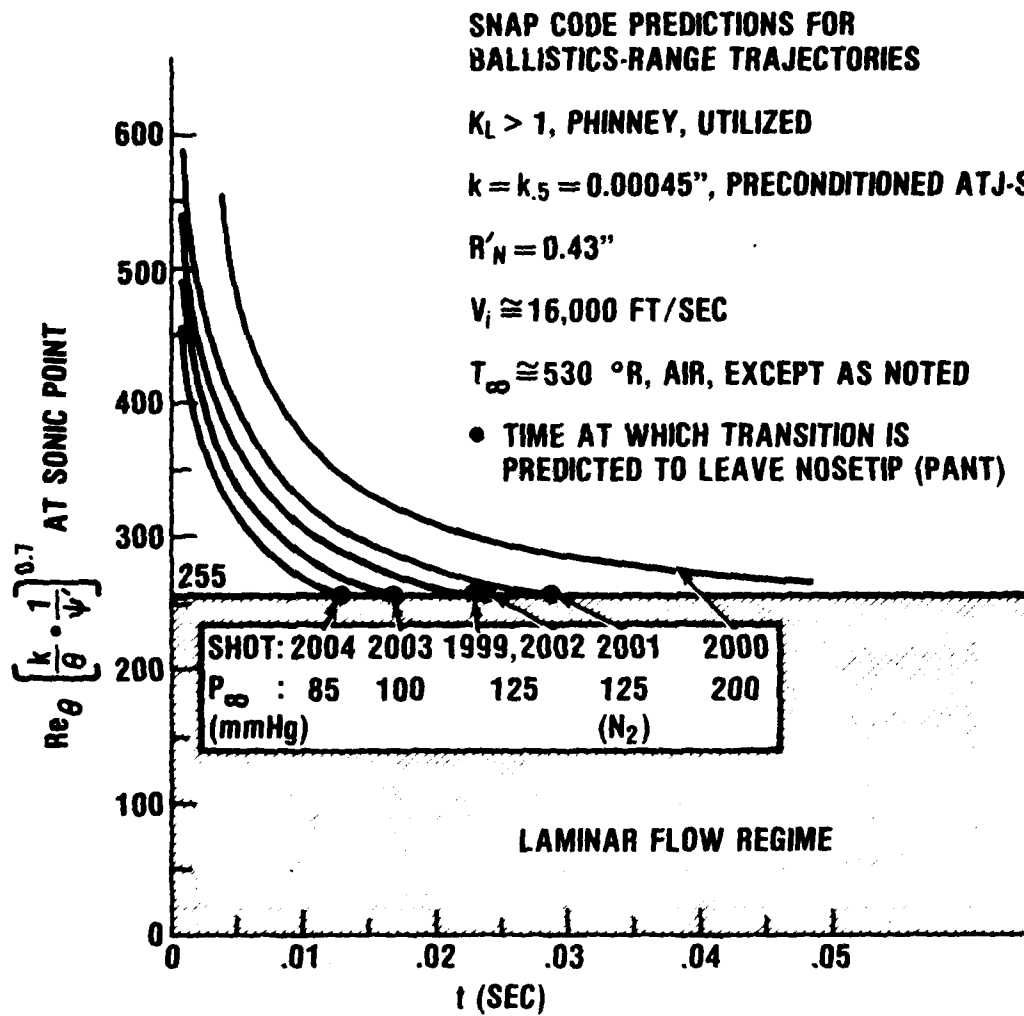
FIG. 6   PANT TRANSITION PARAMETER vs. TIME OF FLIGHT; BALLISTICS RANGE TRA-
JECTORIES, k = .45 MIL

34
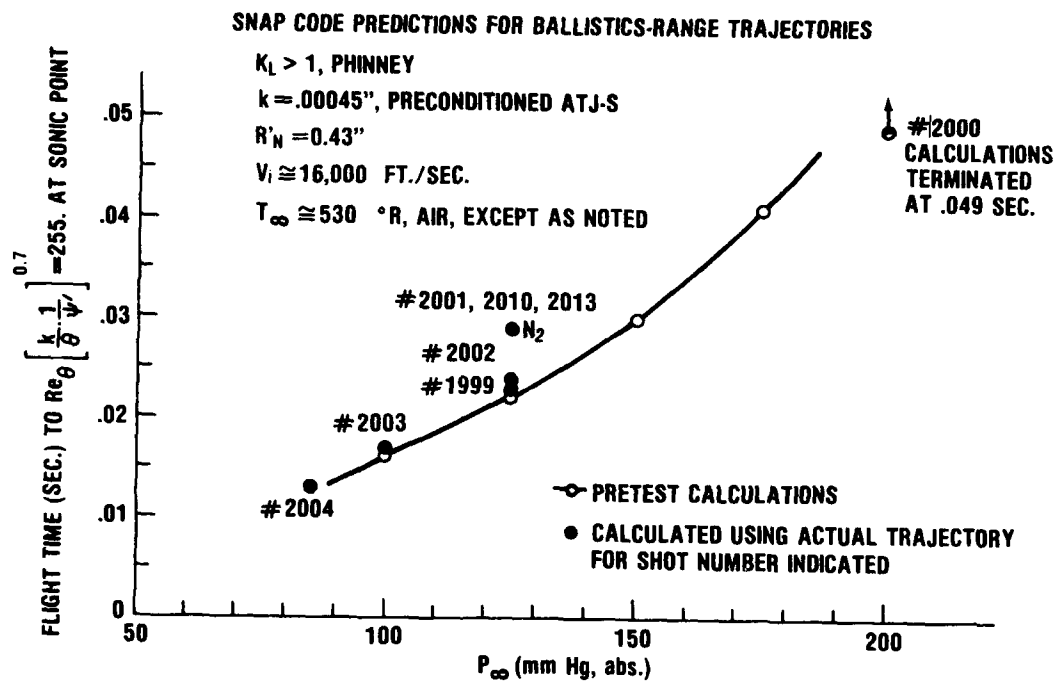
FIG. 7   FLIGHT TIME TO PREDICTED TRANSITION OFFSET vs. RANGE TUBE PRESSURE
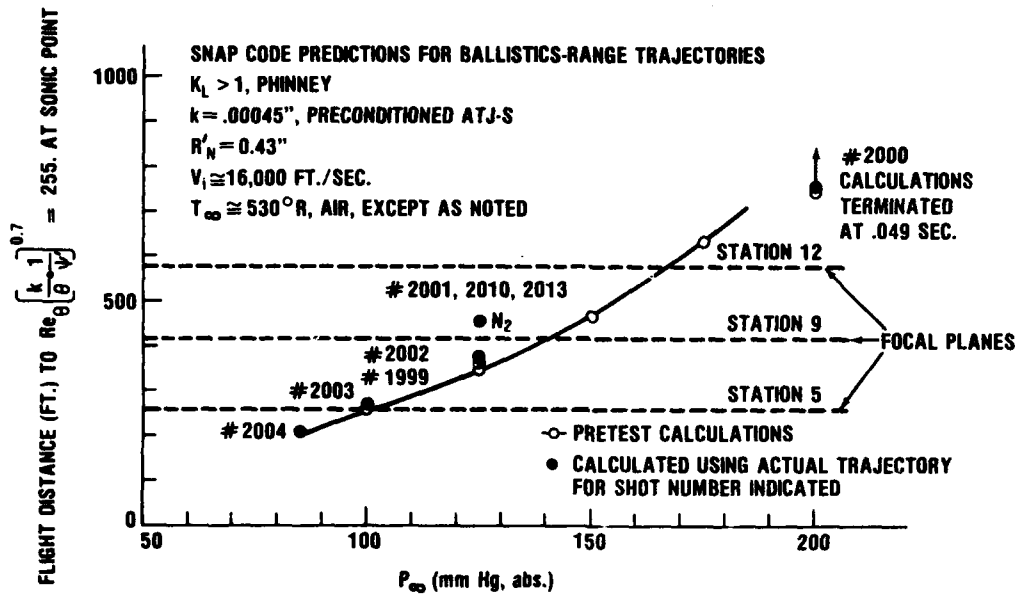
FIG. 8 FLIGHT DISTANCE TO PREDICTED TRANSITION OFFSET vs. RANGE TUBE PRESSURE
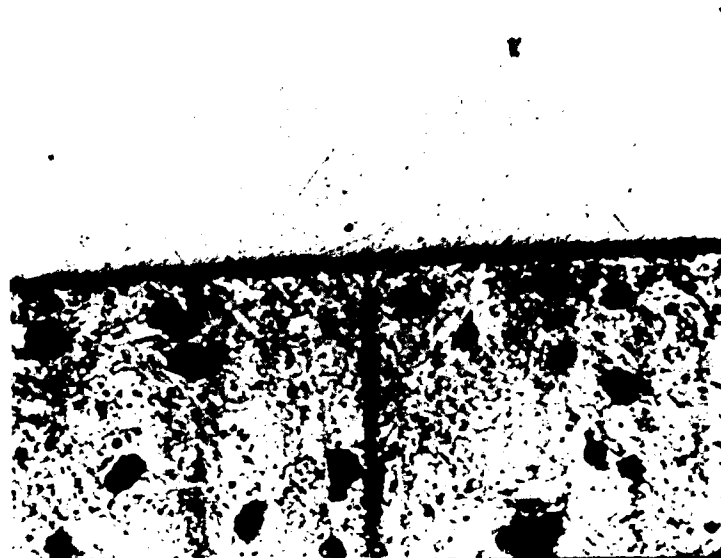
(a) POLISHED

(b) PRECONDITIONED

FIG. 9 320X CROSS-SECTIONAL VIEWS OF POLISHED AND PRECONDITIONED ATJ-S GRAPHITE
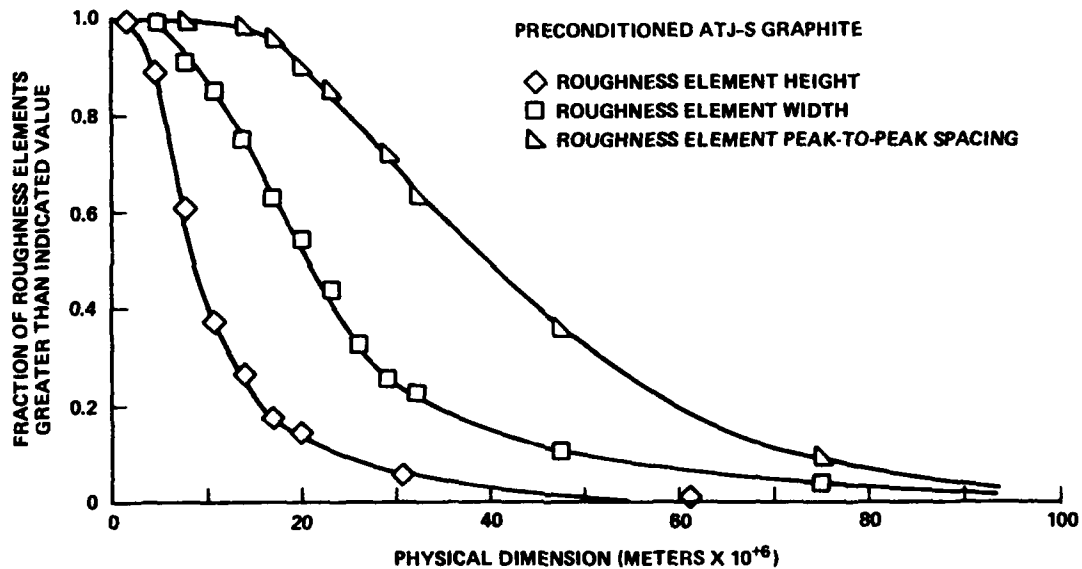
FIG. 10 SURFACE MICROROUGHNESS CHARACTERISTICS OF PRECONDITIONED ATJ-S
GRAPHITE

38
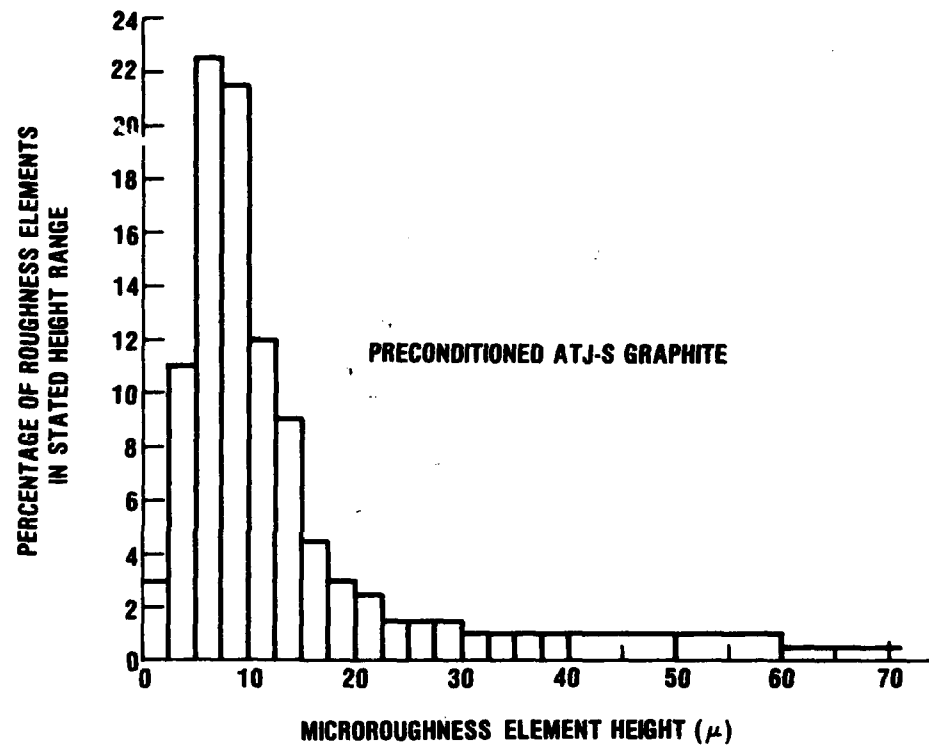
FIG. 11 SURFACE MICROROUGHNESS CHARACTERISTICS OF PRECONDITIONED ATJ-S
GRAPHITE
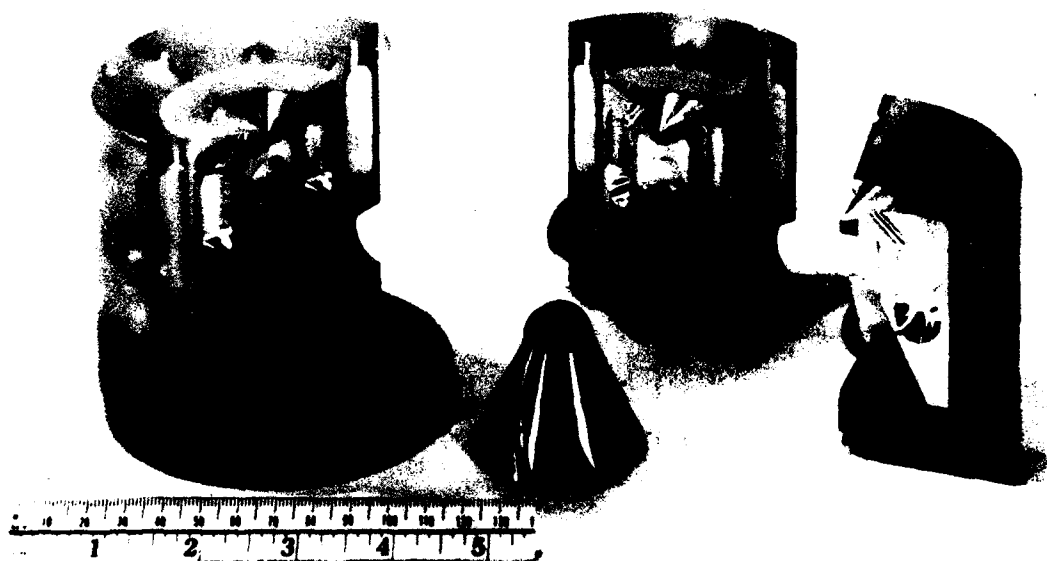
FIG. 12 PHOTOGRAPH OF NOSETIP MODEL AND FULLY ENCLOSED SABOT

TYPICAL RE-ENTRY TRAJECTORIES
FOR SLENDER BLUNTED CONES

CAPABILITY OF N.S.W.C./W.O.L. 1000-FT. RANGE

EFFECTIVE ALTITUDE BASED ON DENSITY

$(P_\infty = 0.5$ mm Hg, $T_\infty = 530$ °R$)$

RE-ENTRY VELOCITY

————— 24,000 FT./SEC.

------ 20,000 FT./SEC.

RE-ENTRY ANGLE = 35°

β AS SHOWN (#$_f$ /FT.^{2})

$\beta = 500$

1000

2000

EFFECTIVE ALTITUDE (KFT.)

V_∞ (KFT./SEC.)
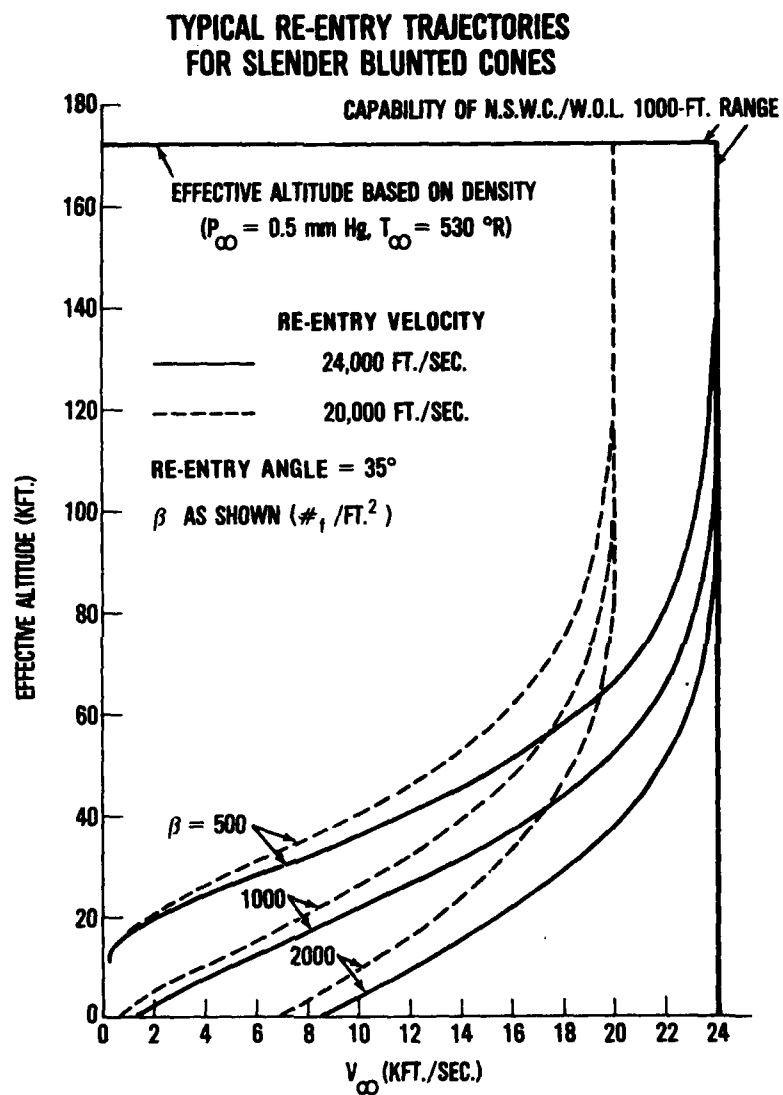
FIG. 13 OPERATING ENVELOPE OF 1000-FOOT BALLISTICS RANGE IN COMPARISON WITH
TYPICAL REENTRY TRAJECTORIES FOR SLENDER BLUNTED CONES

41
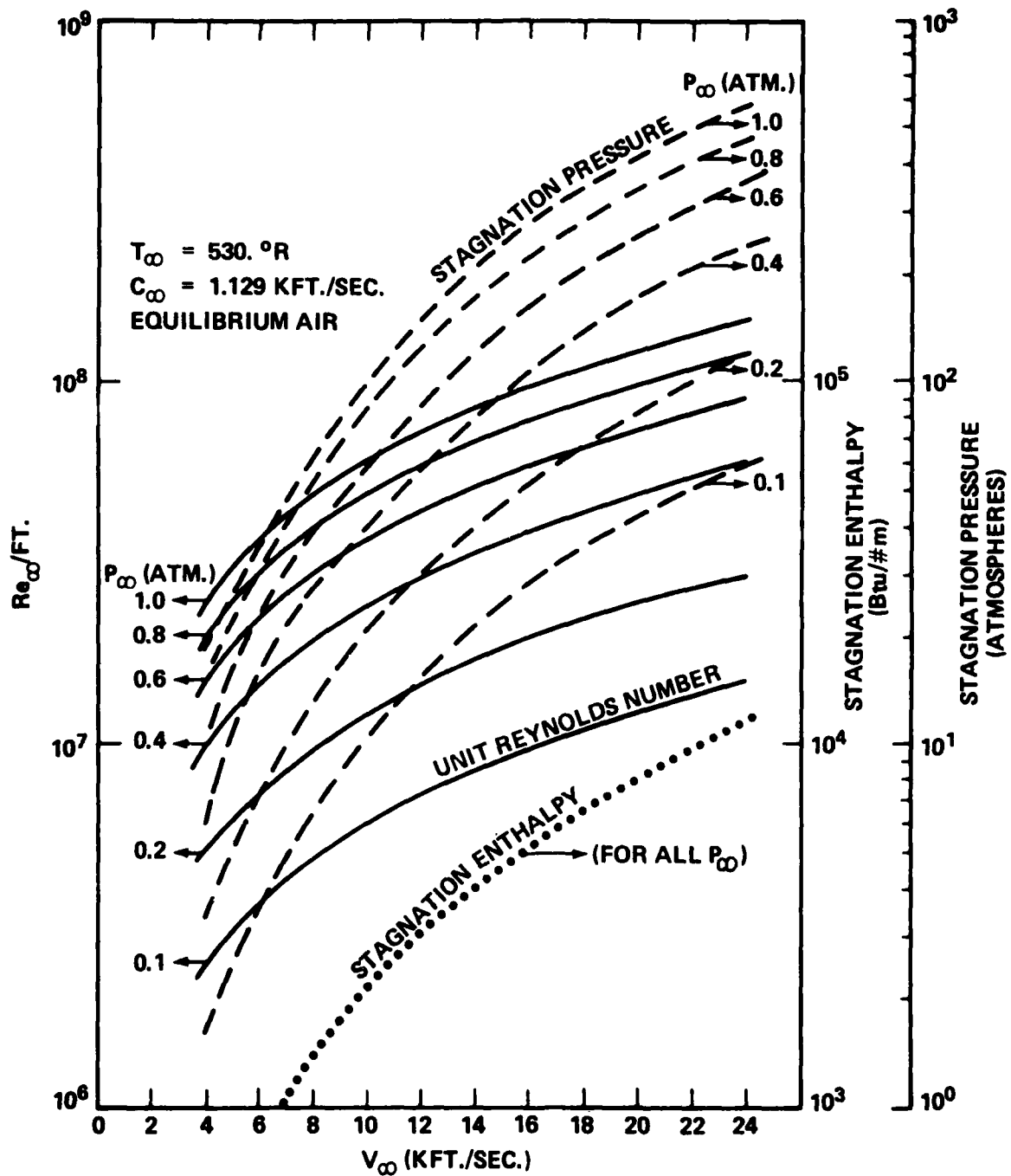
FIG. 14   AEROTHERMODYNAMIC CAPABILITIES OF 1000-FOOT BALLISTICS RANGE
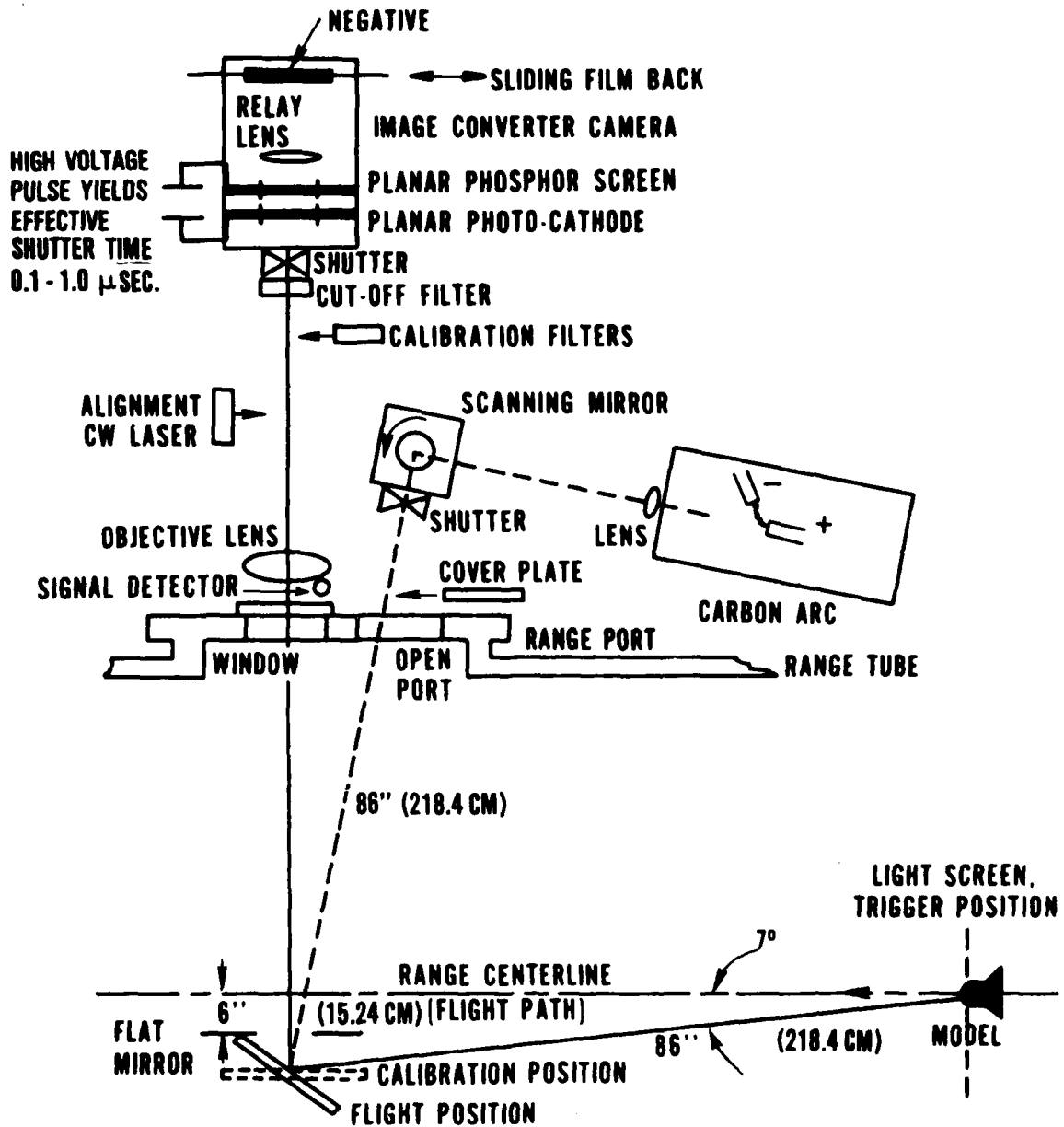
FIG. 15   ELECTRO-OPTICAL PYROMETER SYSTEM SCHEMATIC
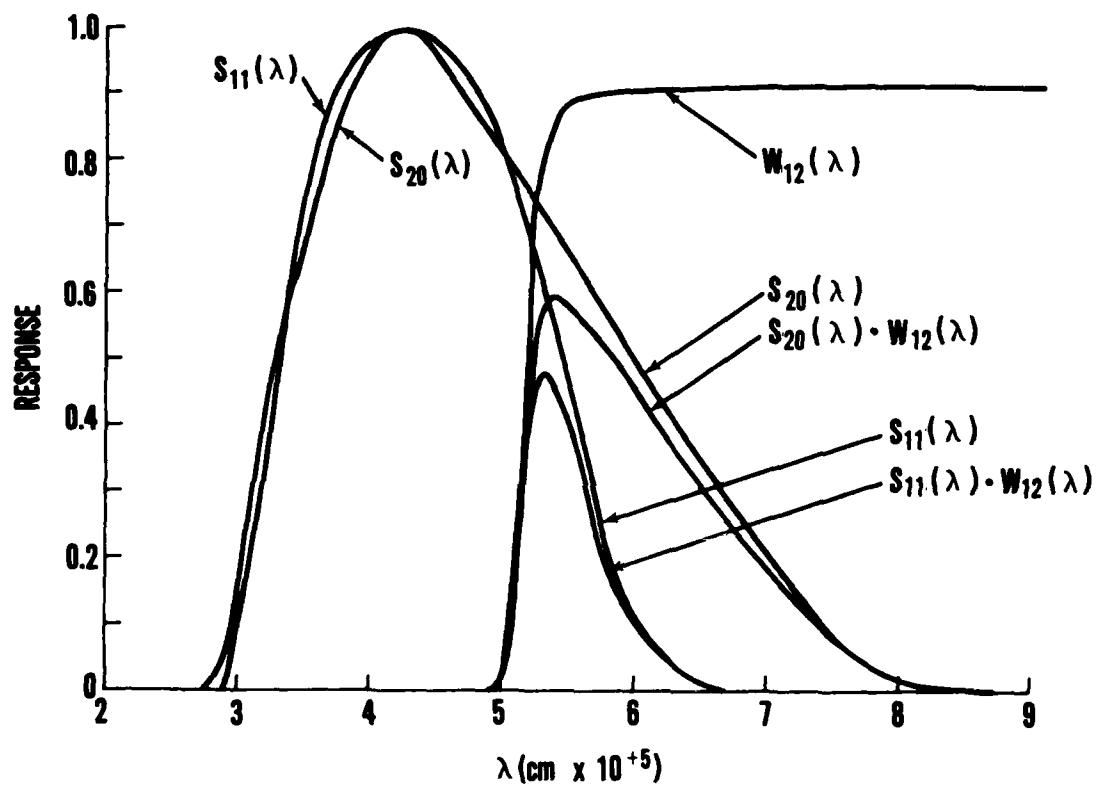
FIG. 16   COMPONENT AND OVERALL SYSTEM WAVELENGTH RESPONSE
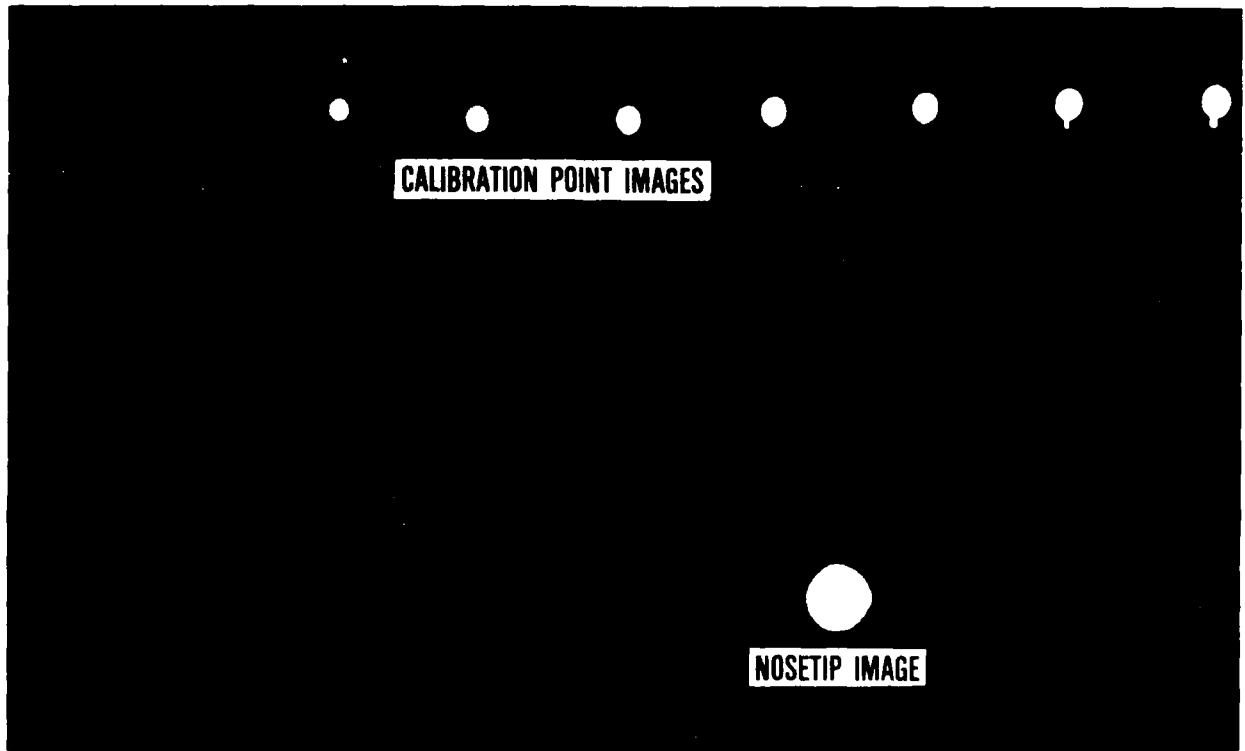
FIG. 17 PRINT OF DATA NEGATIVE
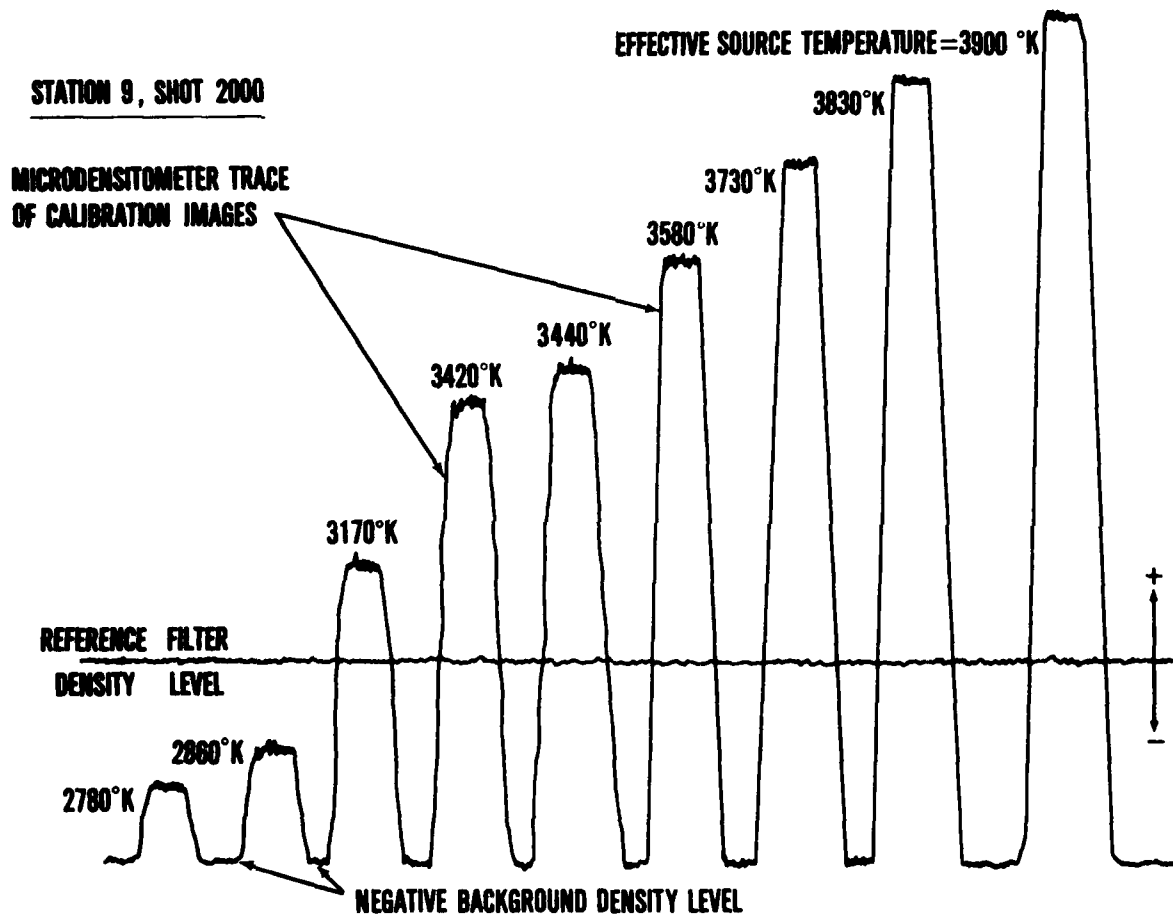
FIG. 18   MICRODENSITOMETER TRACE OF CALIBRATION IMAGES
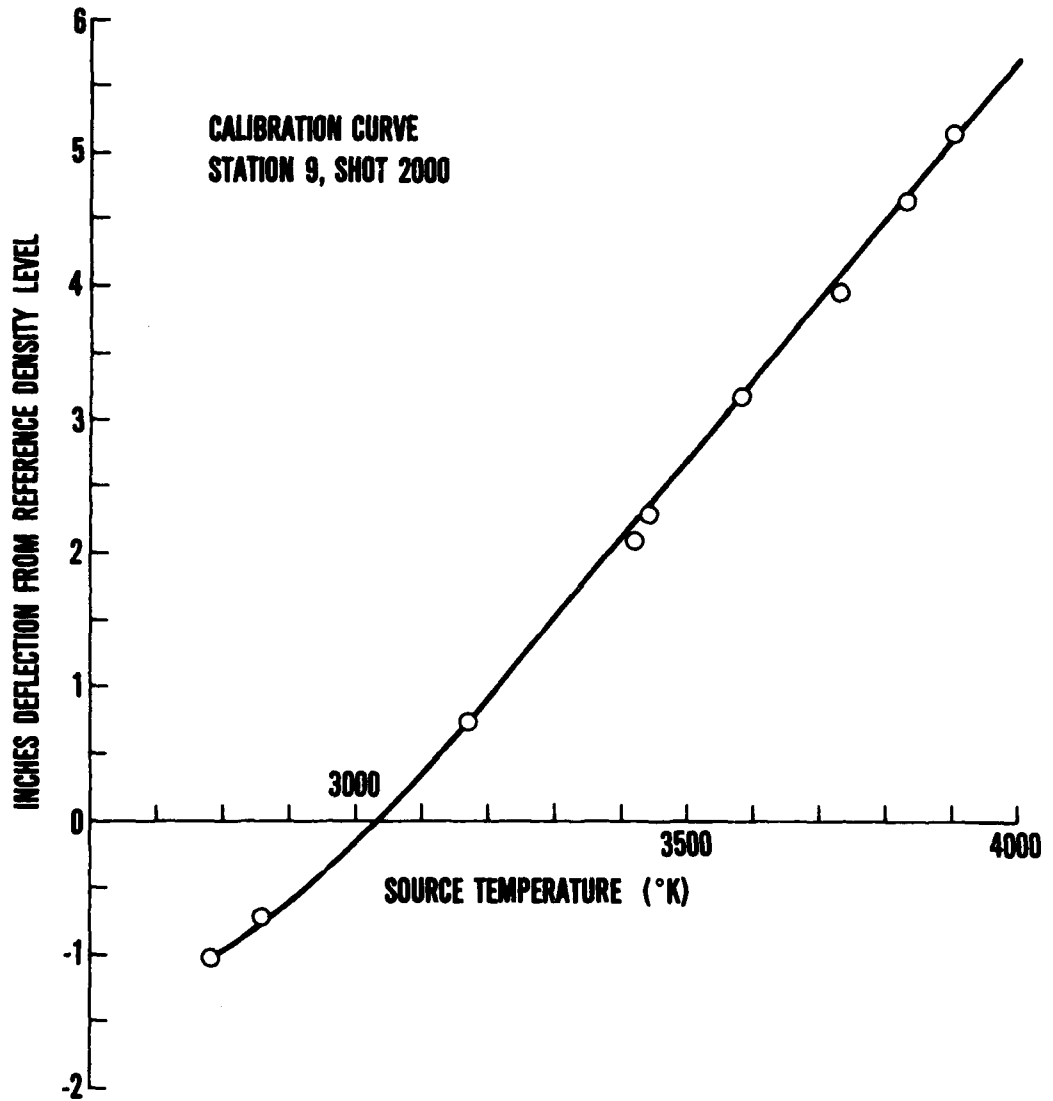
FIG. 19 PYROMETER SYSTEM CALIBRATION CURVE
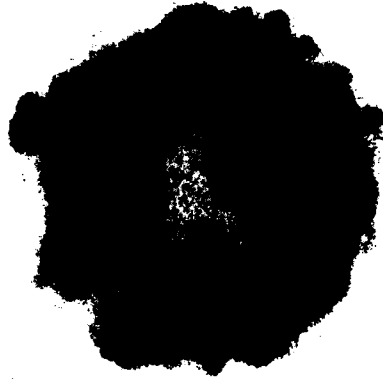
SHOT 2003, STATION 5
P_∞ = 100. mm Hg, abs.
TRANSITIONAL FLOW
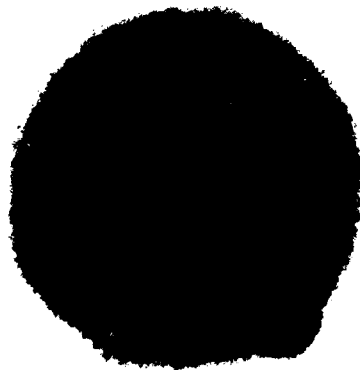
SHOT 2000, STATION 5
P_∞ = 200. mm Hg, abs.
TURBULENT FLOW

FIG. 20 DATA NEGATIVES ILLUSTRATING TRANSITIONAL AND TURBULENT FLOW

48
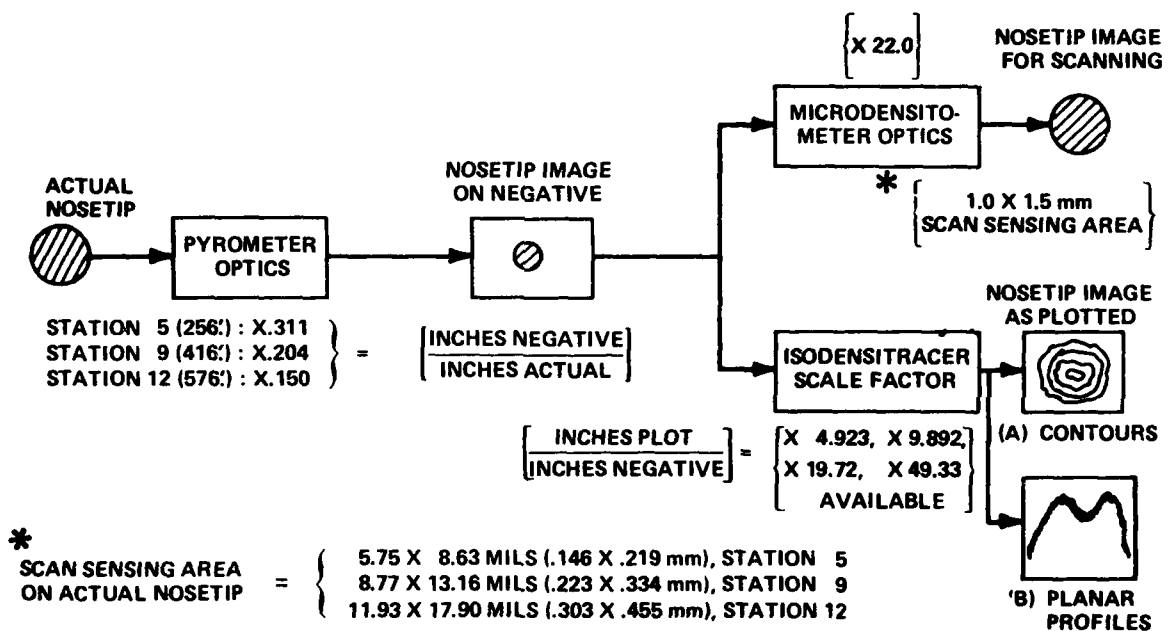
FIG. 21   SCHEMATIC OF OPTICAL AND MECHANICAL MAGNIFICATION FACTORS

FIG. 22   AIR RADIATION

50

$$E_b (\lambda) = \left(\frac{C_1}{\lambda^5}\right) \left[\frac{1}{EXP. \ (C_2/\lambda T) - 1}\right]$$

$C_1 = 3.7403 \times 10^{-12}$ WATTS - CM^2

$C_2 = 2.5897$ CM - ^{0}R = 1.4387 CM - ^{0}K

$T = 7000. \ ^0$R = 3889. ^{0}K

$\epsilon = 0.9$

$[\epsilon E_b (\lambda)]$

$[\epsilon E_b (\lambda) S_{11} (\lambda)]$

$[\epsilon E_b (\lambda) S_{11} (\lambda) W_{12} (\lambda)]$

(WATTS/CM^3) (x 10^{-7})

λ (CM. x 10^{+5})
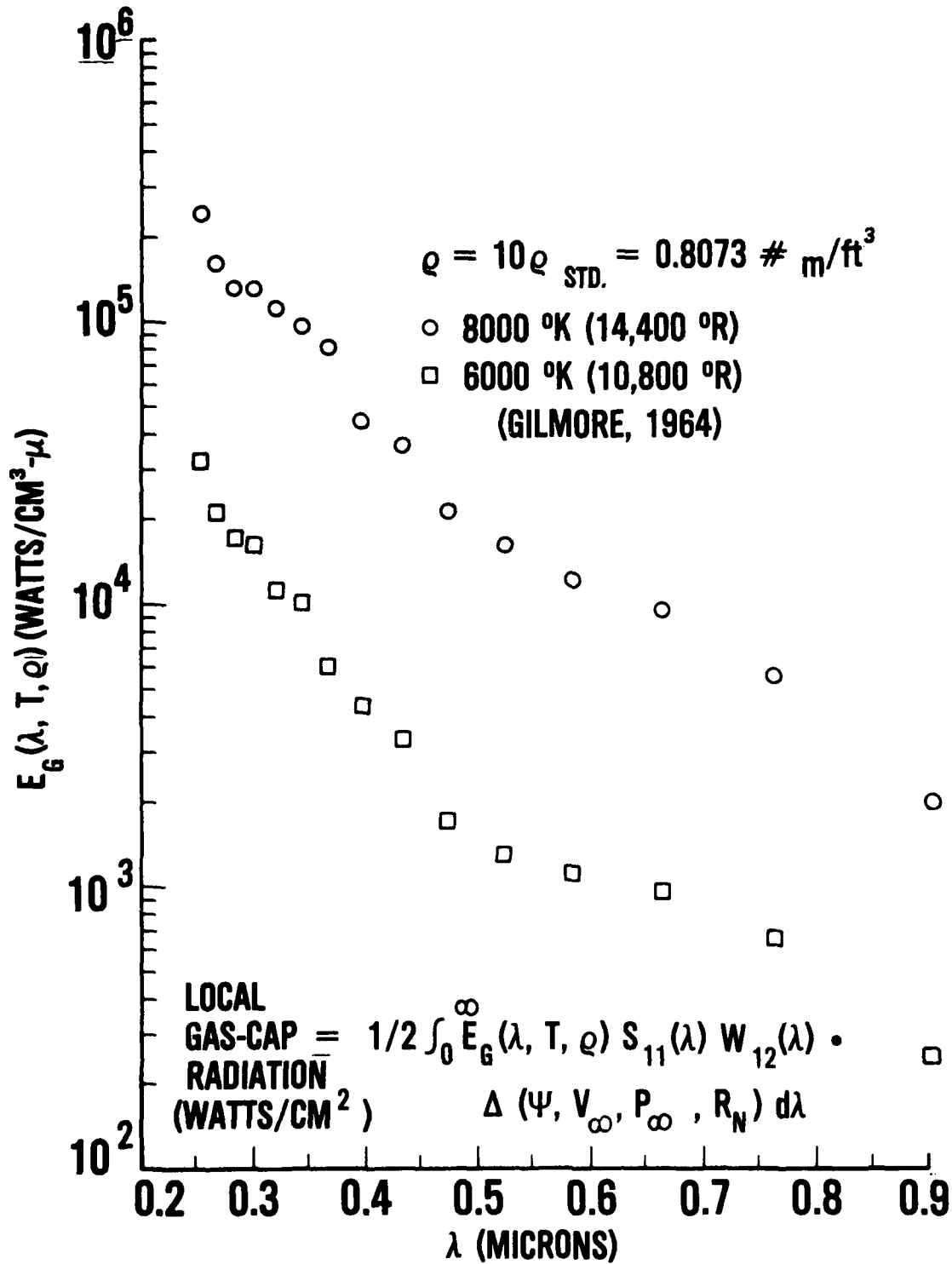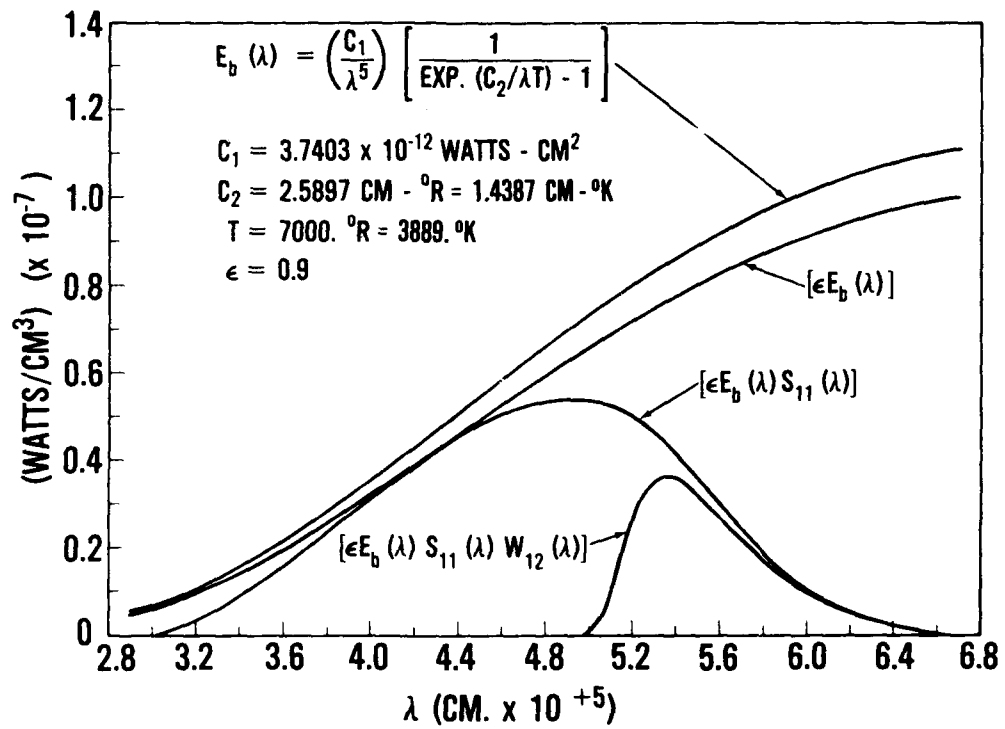
FIG. 23 RESPONSE TO BLACK BODY RADIATION
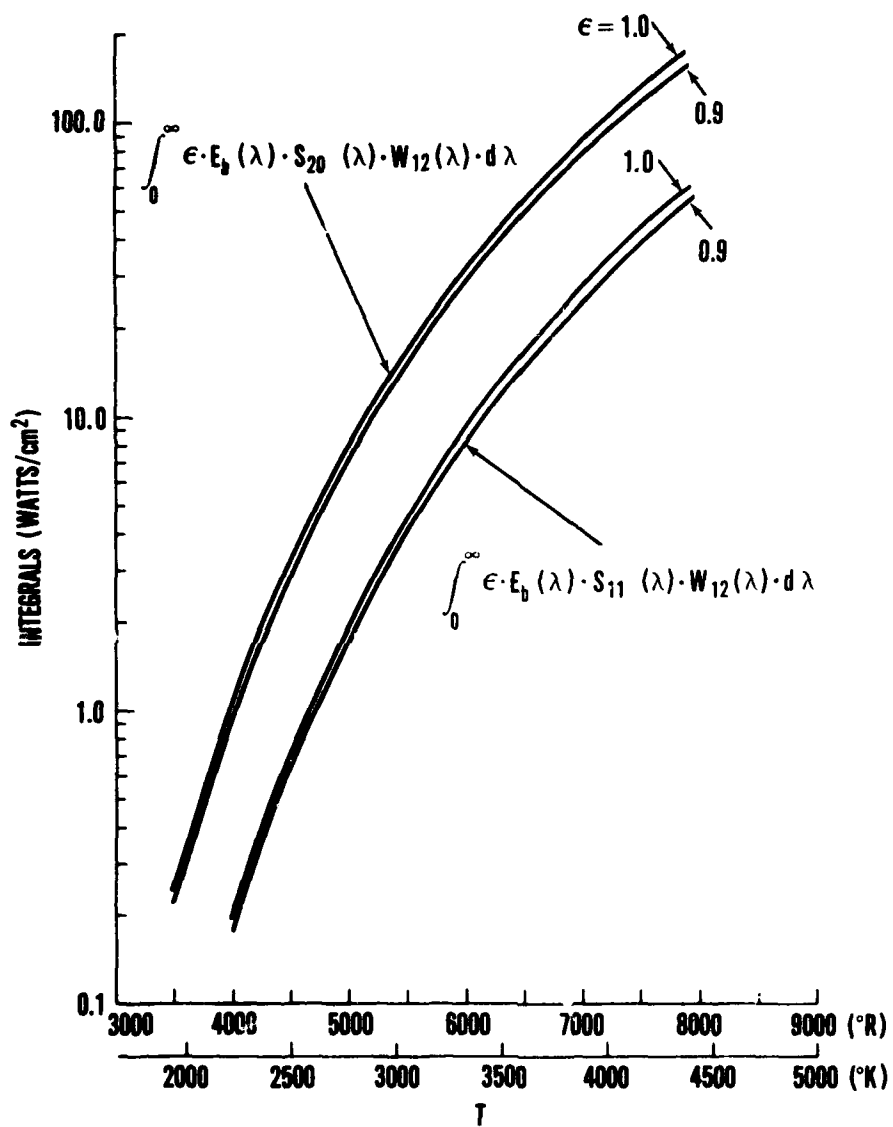
FIG. 24   ENERGY PER UNIT AREA SENSED BY PYROMETERS VS SOURCE TEMPERATURE
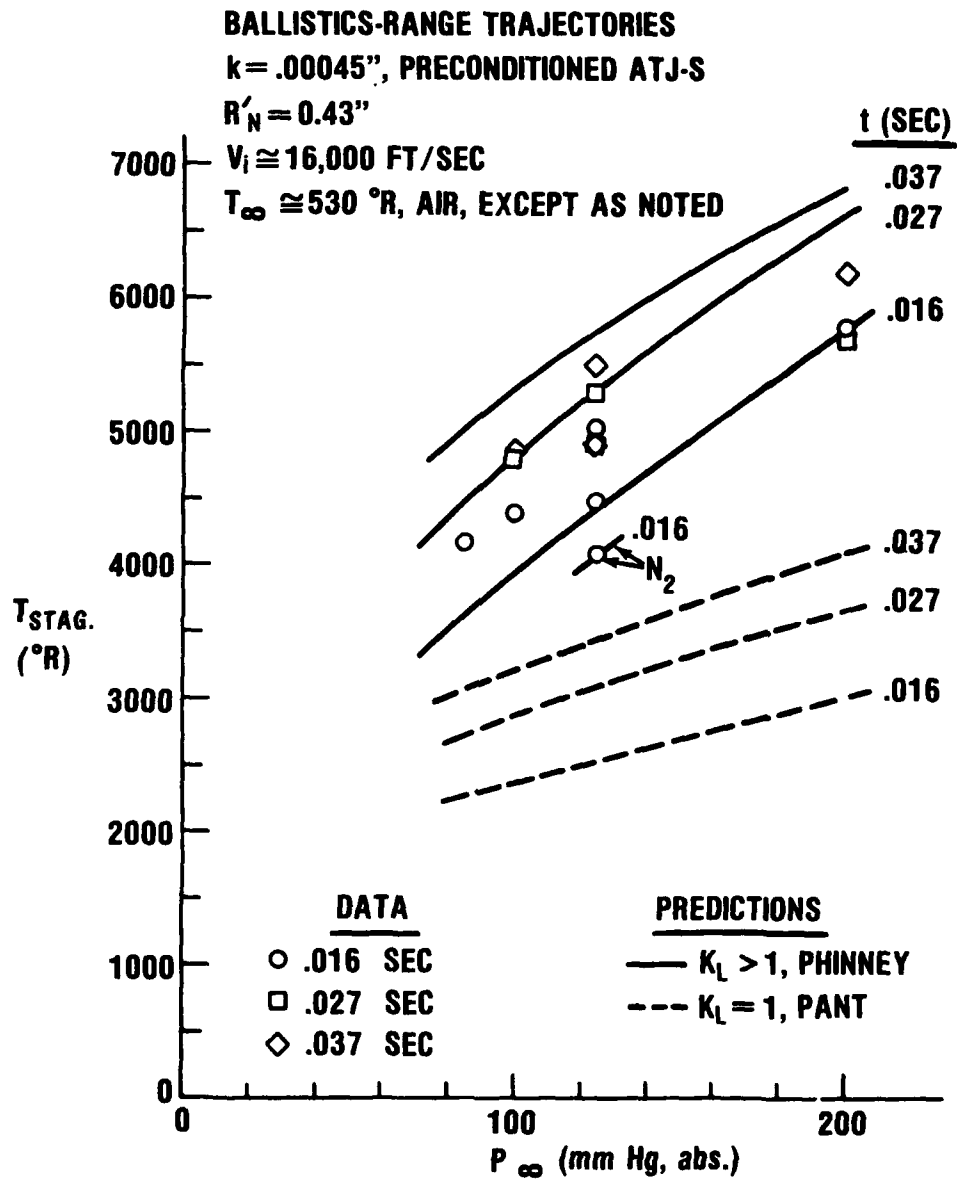
FIG. 25   SURFACE ROUGHNESS EFFECTS ON LAMINAR HEAT-TRANSFER RATES

FIG. 26   AEROTHERMODYNAMIC TRAJECTORY, SHOT 2004

SHOT 2004, STATION 5
t = .016 SEC

○ DATA

—— PREDICTIONS

▨ PREDICTED START OF TRANSITION ZONE, PANT

( ) MICROROUGHNESS FOR TRANSITION
ONSET/LOCATION, MILS

(.78)

(.45)

$K_L > 1$, PHINNEY

(.45)

$K_L = 1$, PANT

TRANSITION PREDICTED
TO LEAVE NOSETIP
AT .013 SEC.

NOTE: AT .027 SEC, ISOLATED HOT SPOTS ~ 4700 - 4800°R
OBSERVED; INSUFFICIENT DETAIL TO PLOT.
AT .037 SEC, NO DATA; MODEL DISPERSION.

SONIC POINT

T (°R)

(S/R_N)
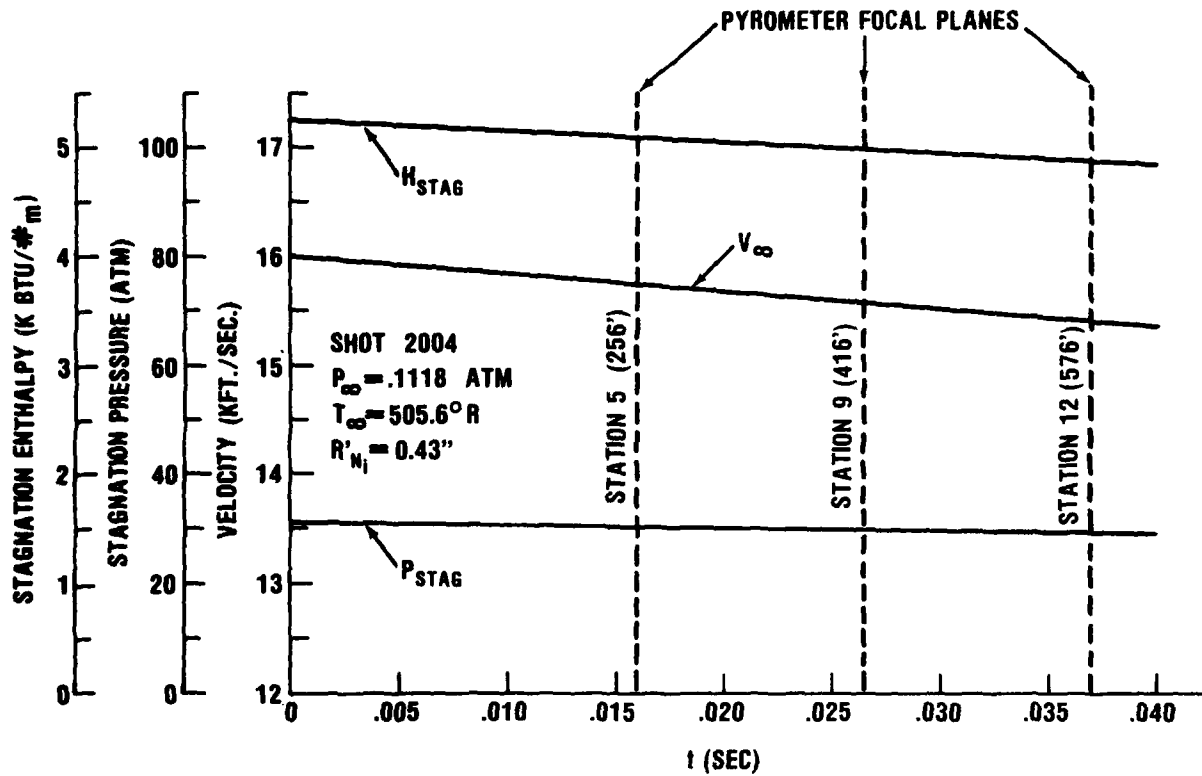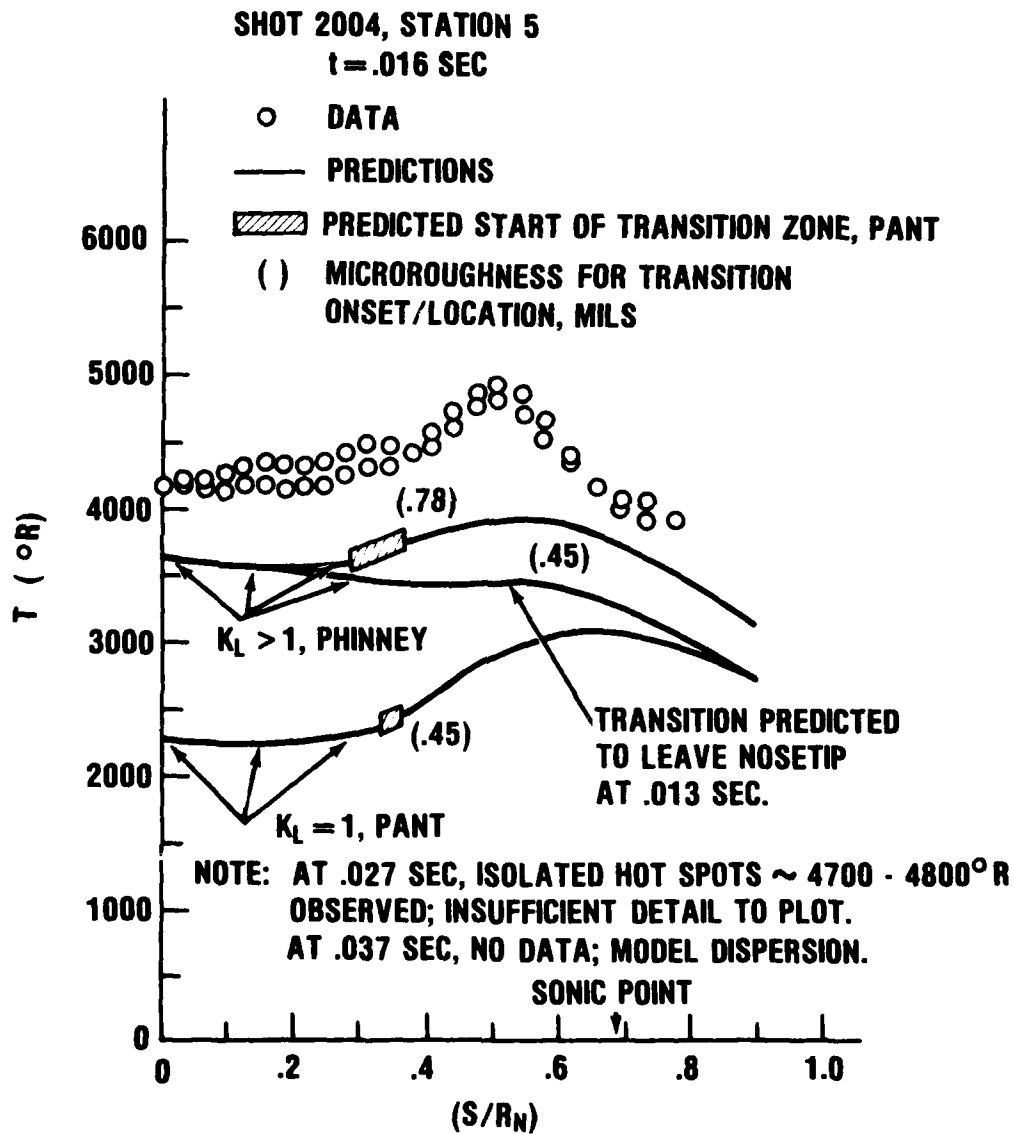
FIG. 27   T vs. (S/R_n), SHOT 2004, .016 SEC.

55
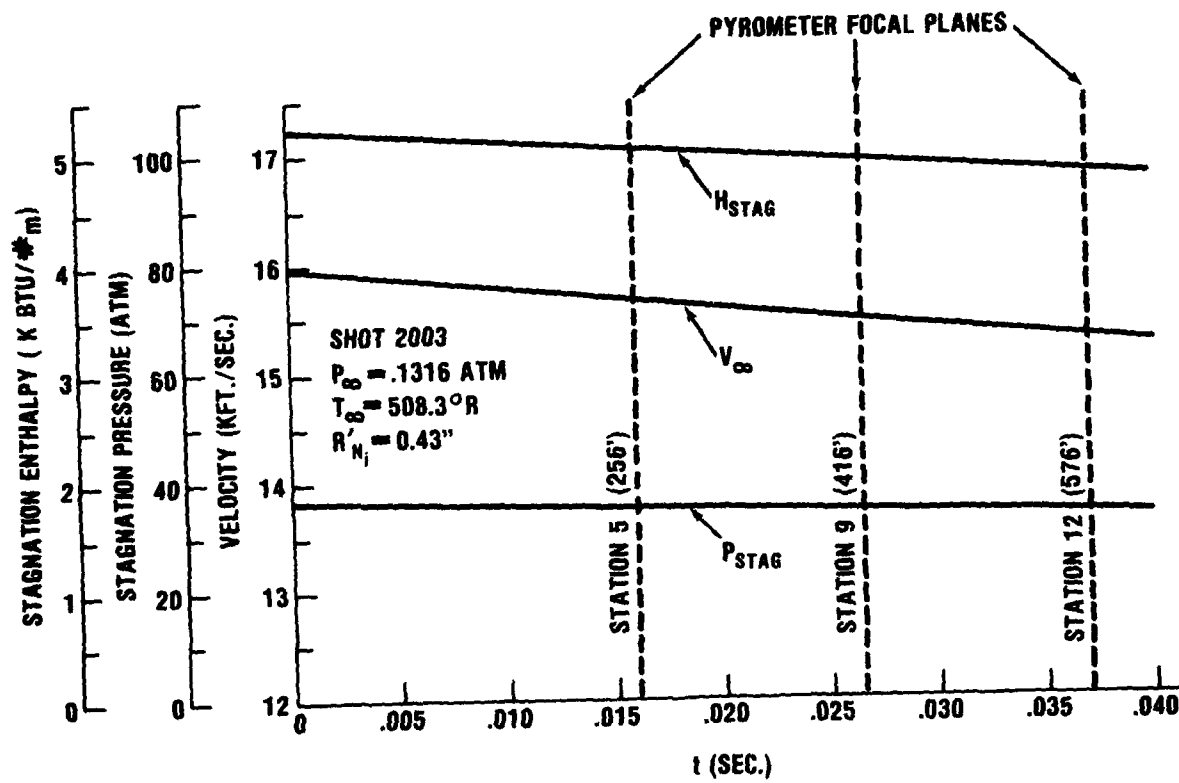
FIG. 28   AEROTHERMODYNAMIC TRAJECTORY, SHOT 2003
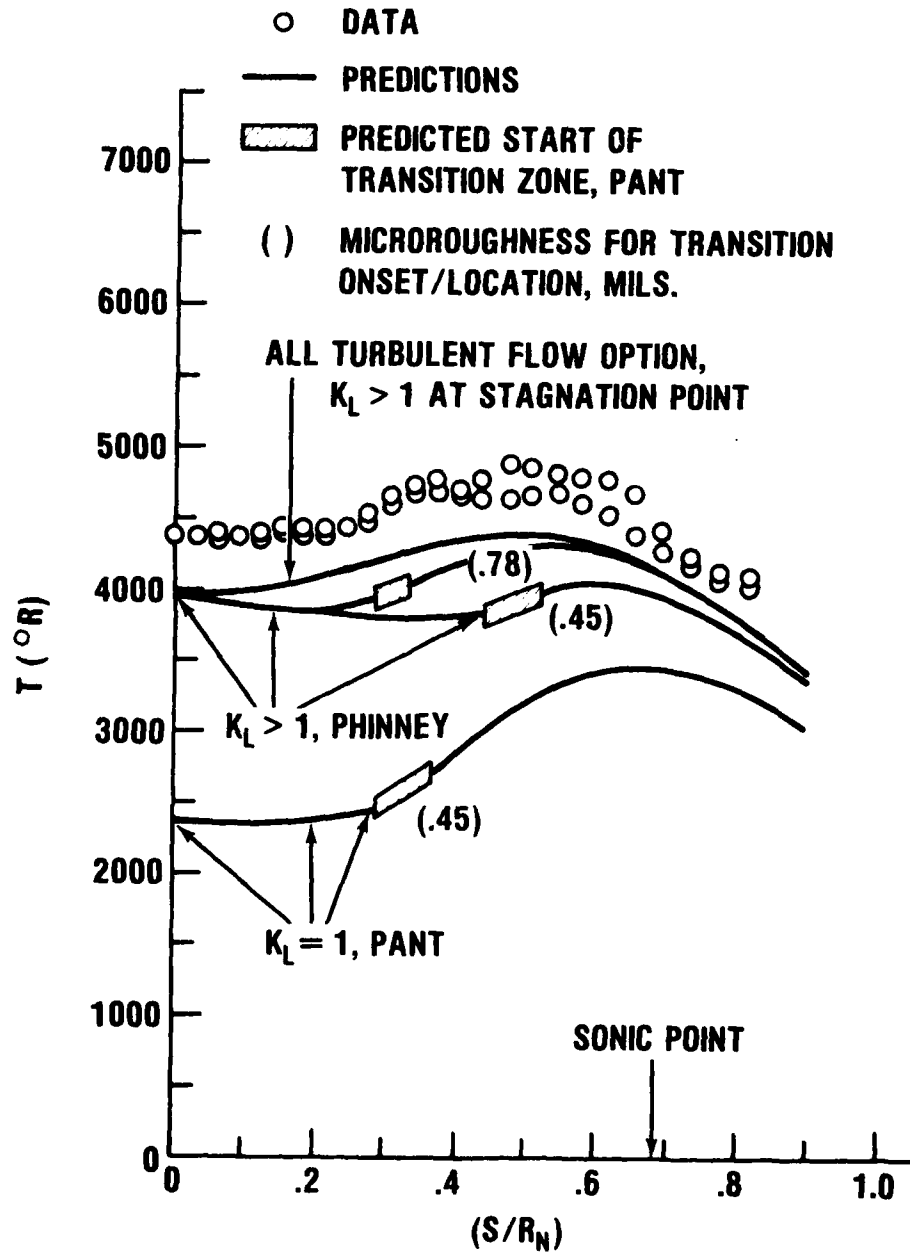
FIG. 29   T vs. (S/R$_n$), SHOT 2003, .016 SEC.
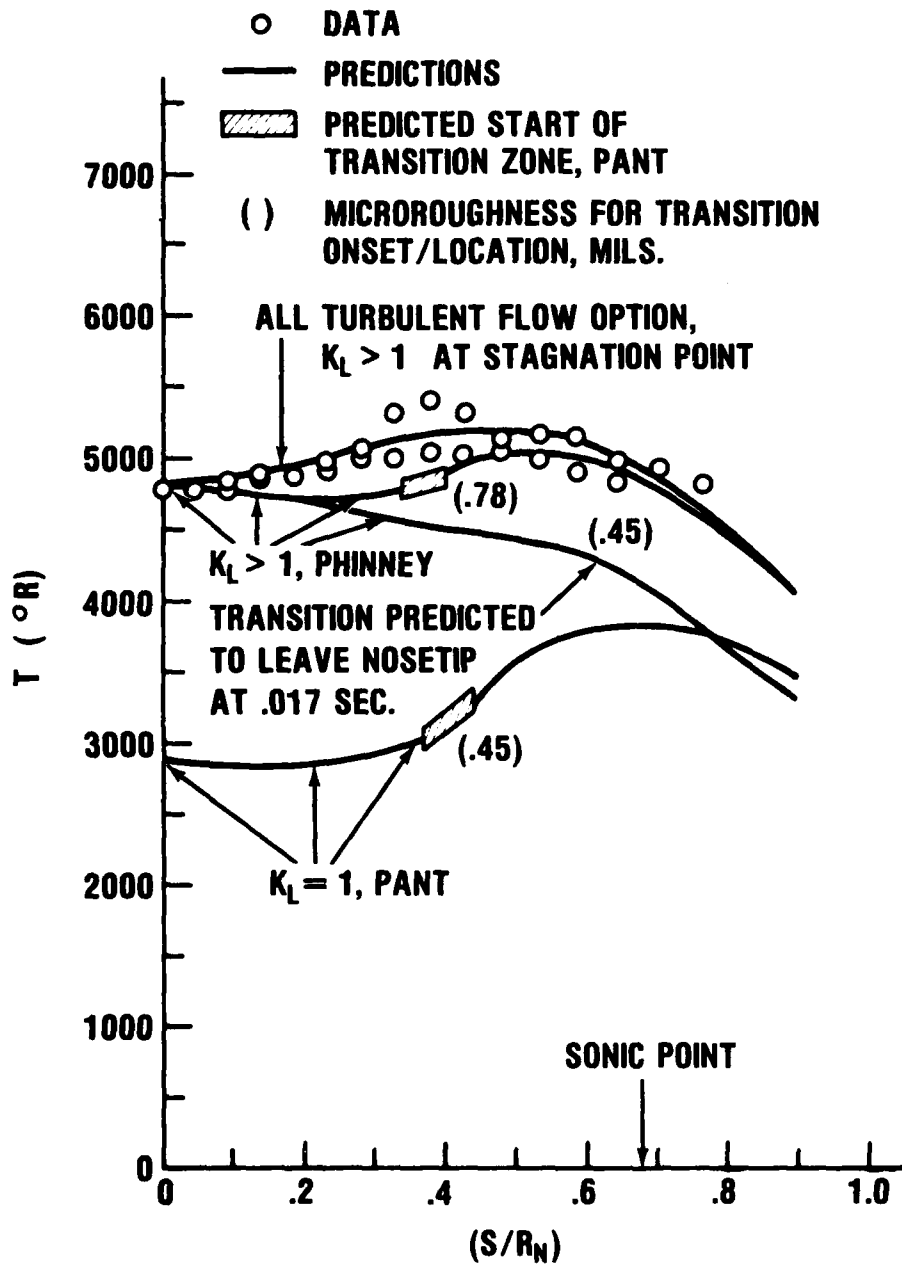
FIG. 30   T vs. (S/R_n), SHOT 2003, .027 SEC.
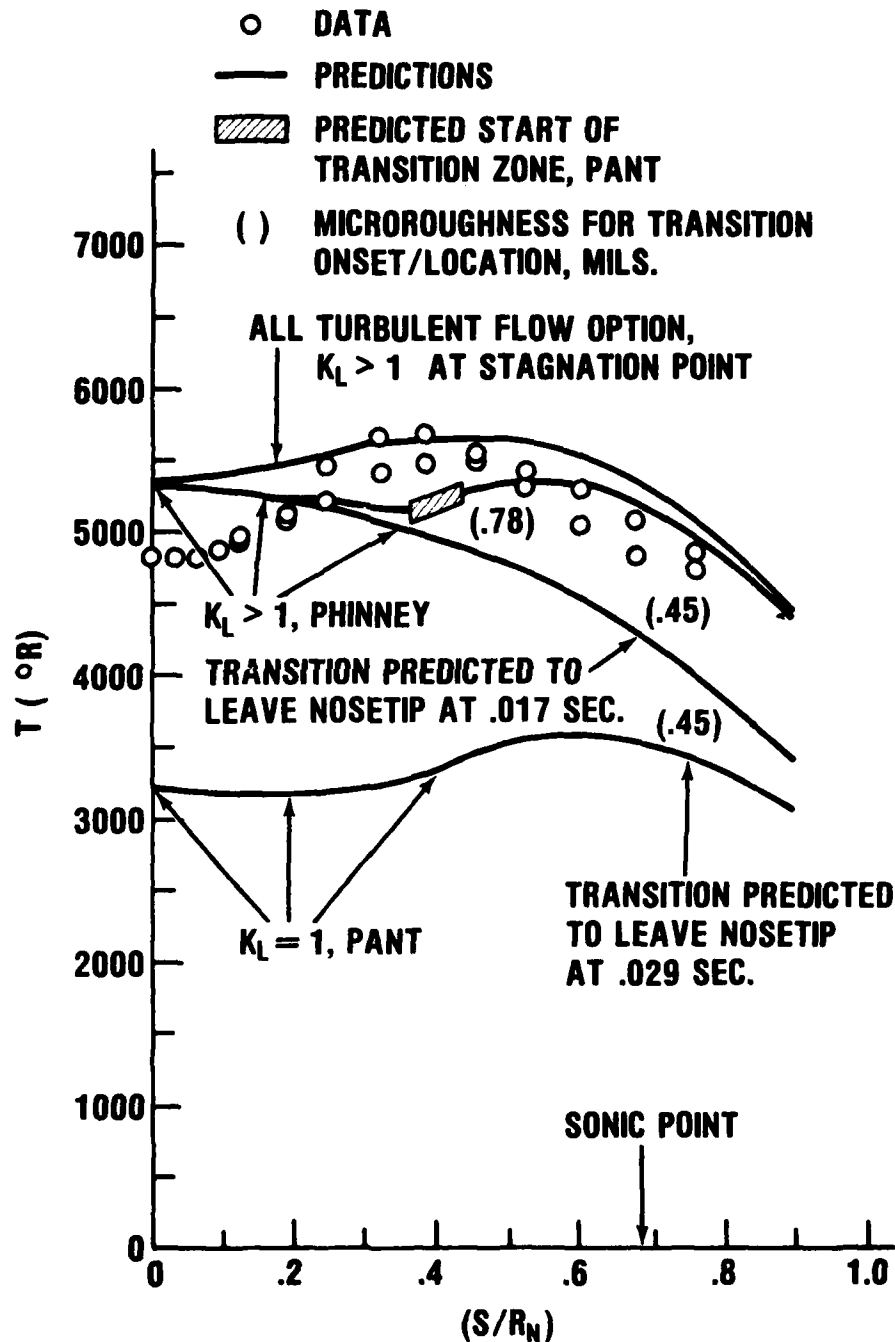
FIG. 31   T vs. (S/R$_n$), SHOT 2003, .037 SEC.
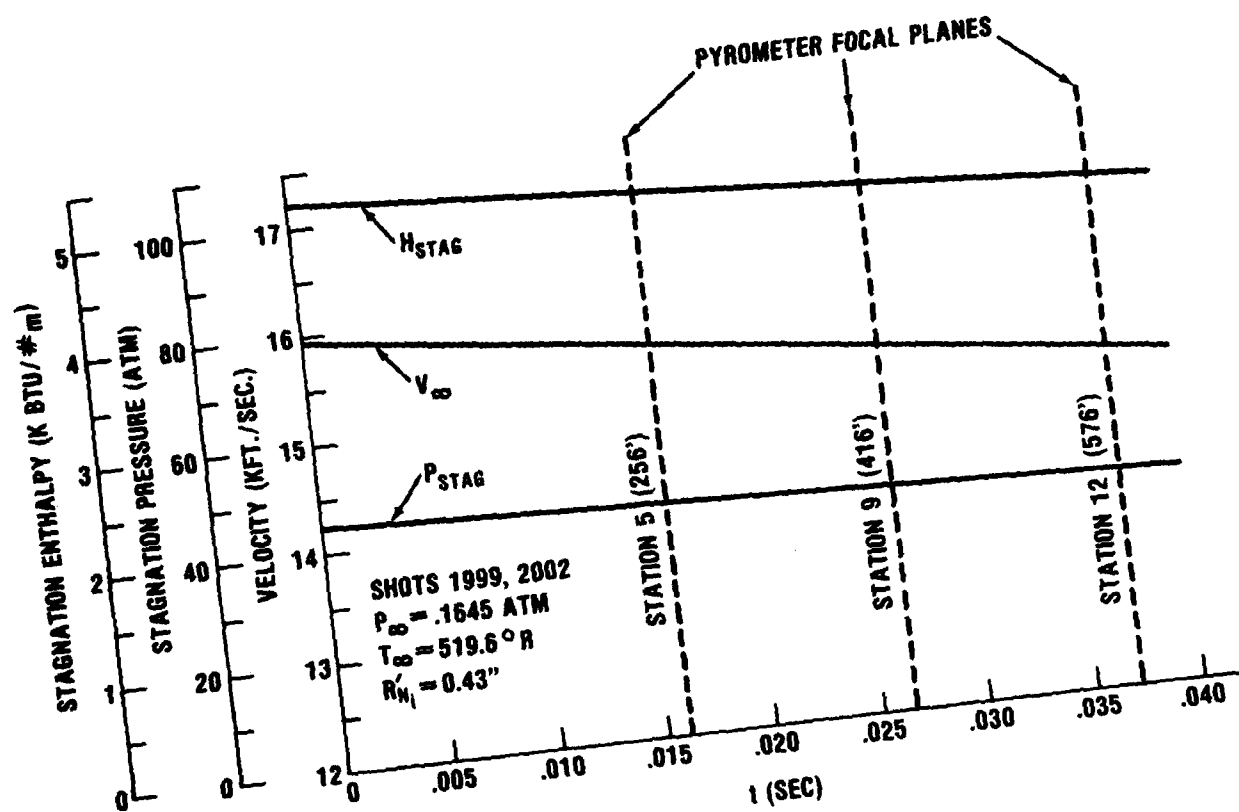
FIG. 32   AEROTHERMODYNAMIC TRAJECTORY, SHOTS 1999, 2002
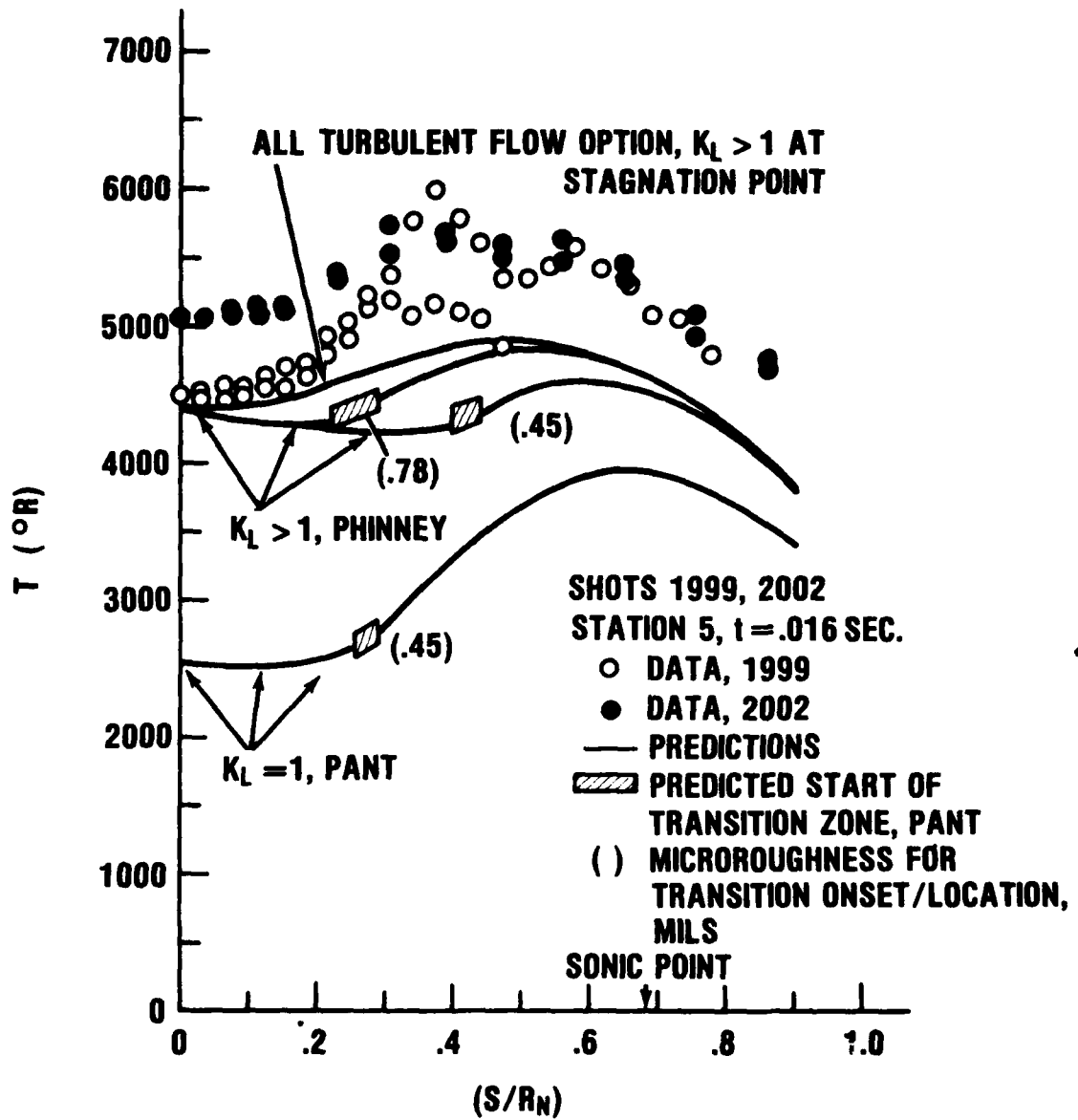
FIG. 33   T vs. (S/R_n), SHOTS 1999, 2002, .016 SEC.
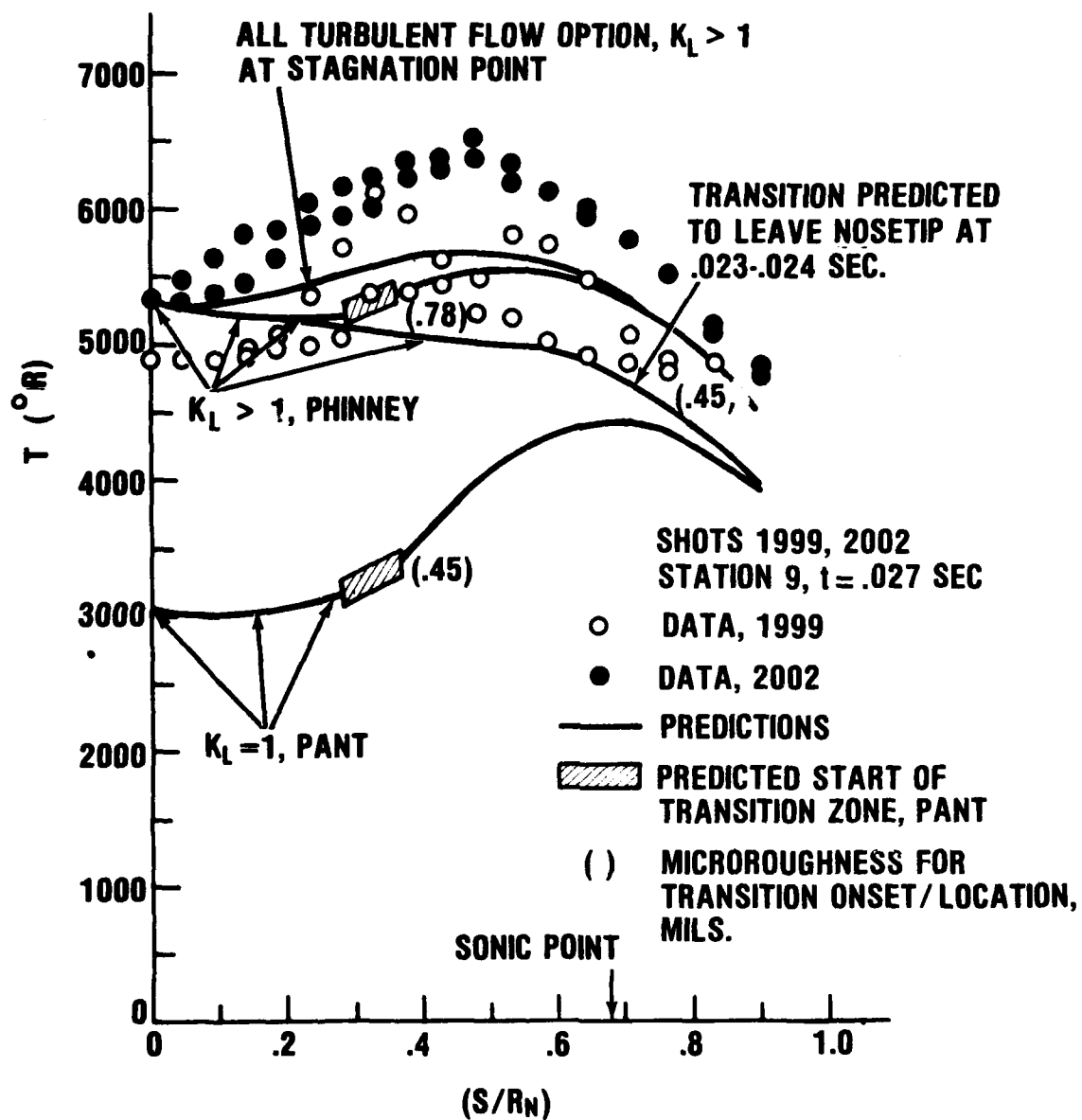
FIG. 34   T vs (S/R$_n$), SHOTS 1999, 2002, .027 SEC.
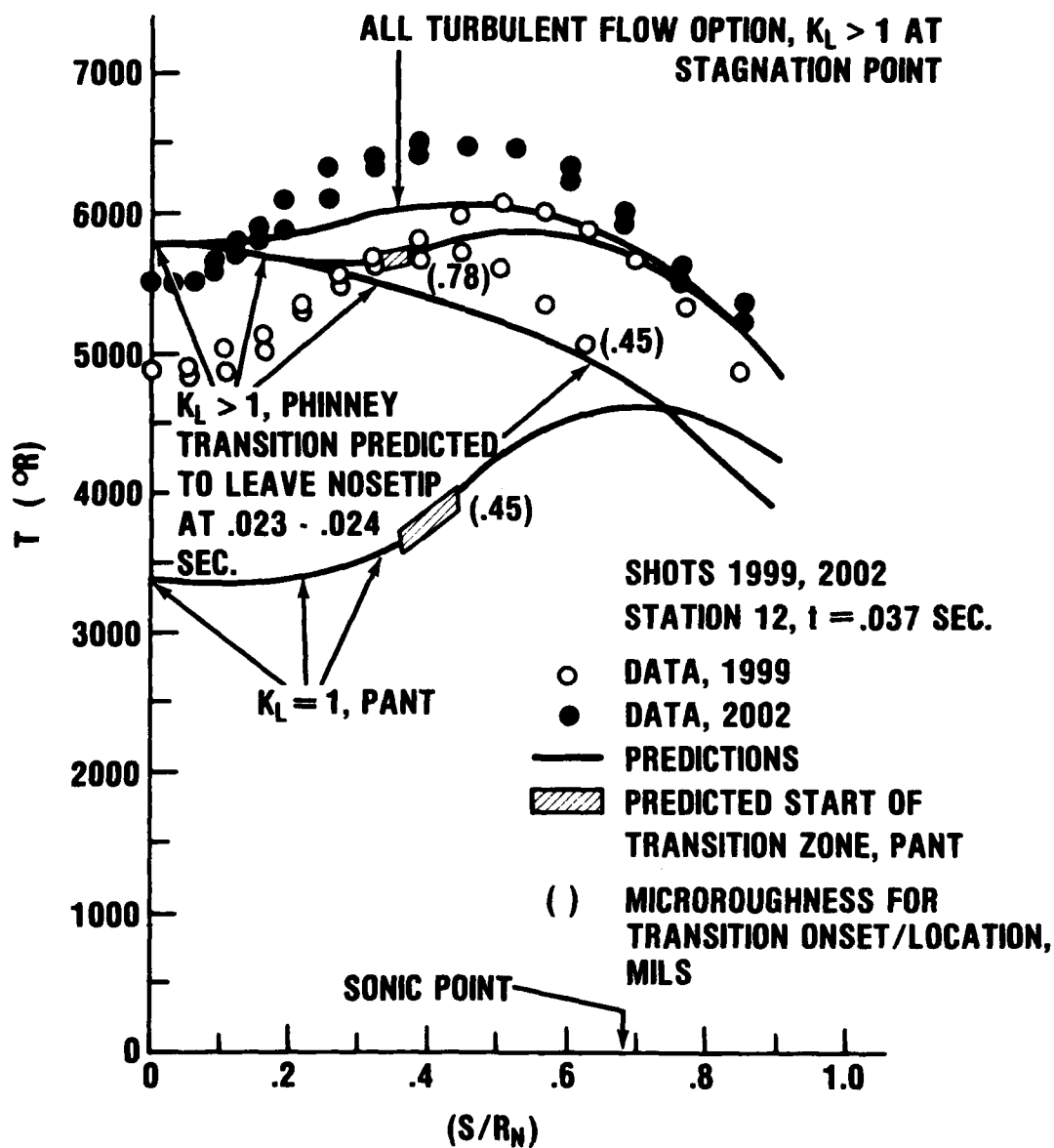
FIG. 35   T vs. (S/R$_n$), SHOTS 1999, 2002, .037 SEC.
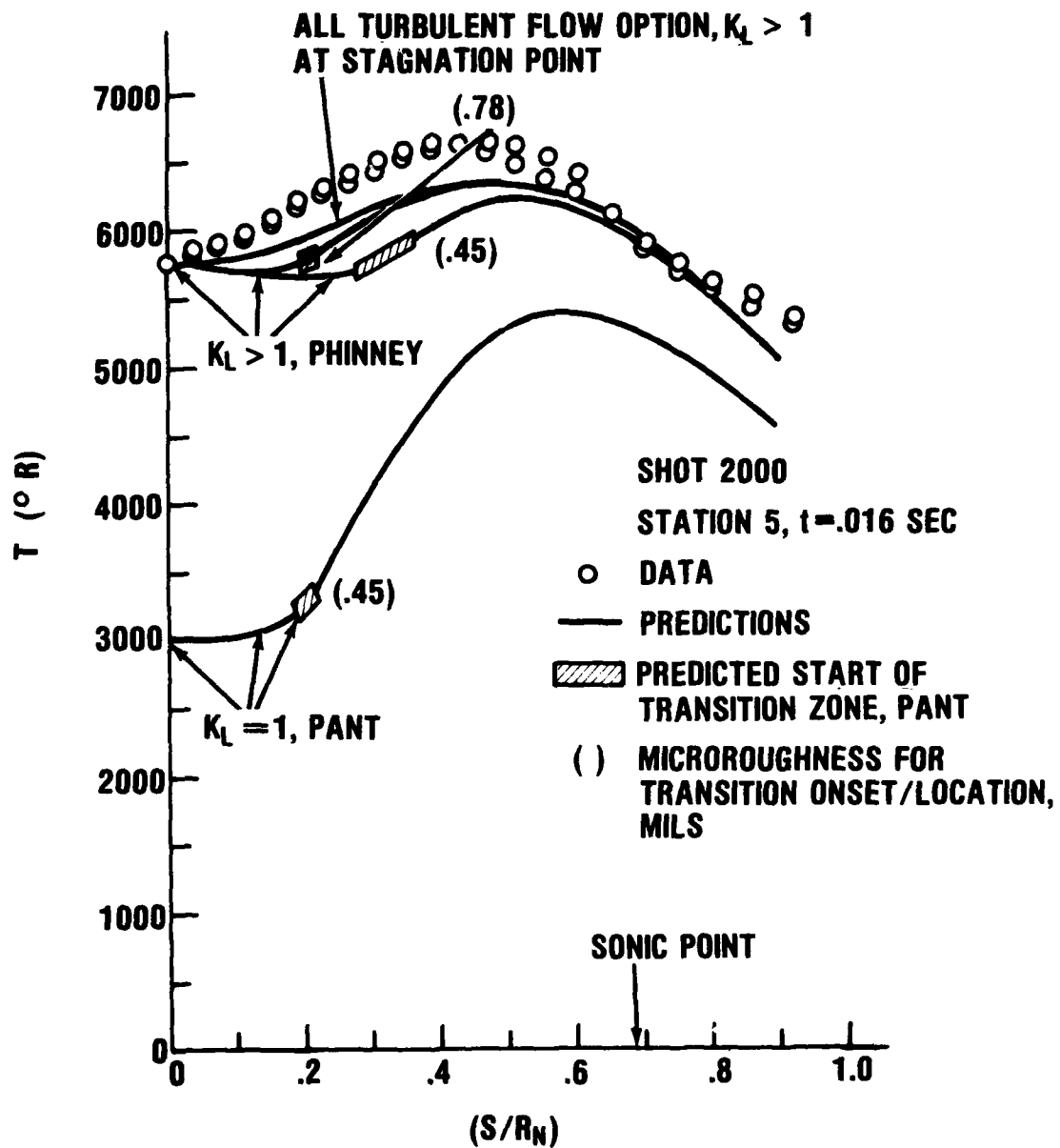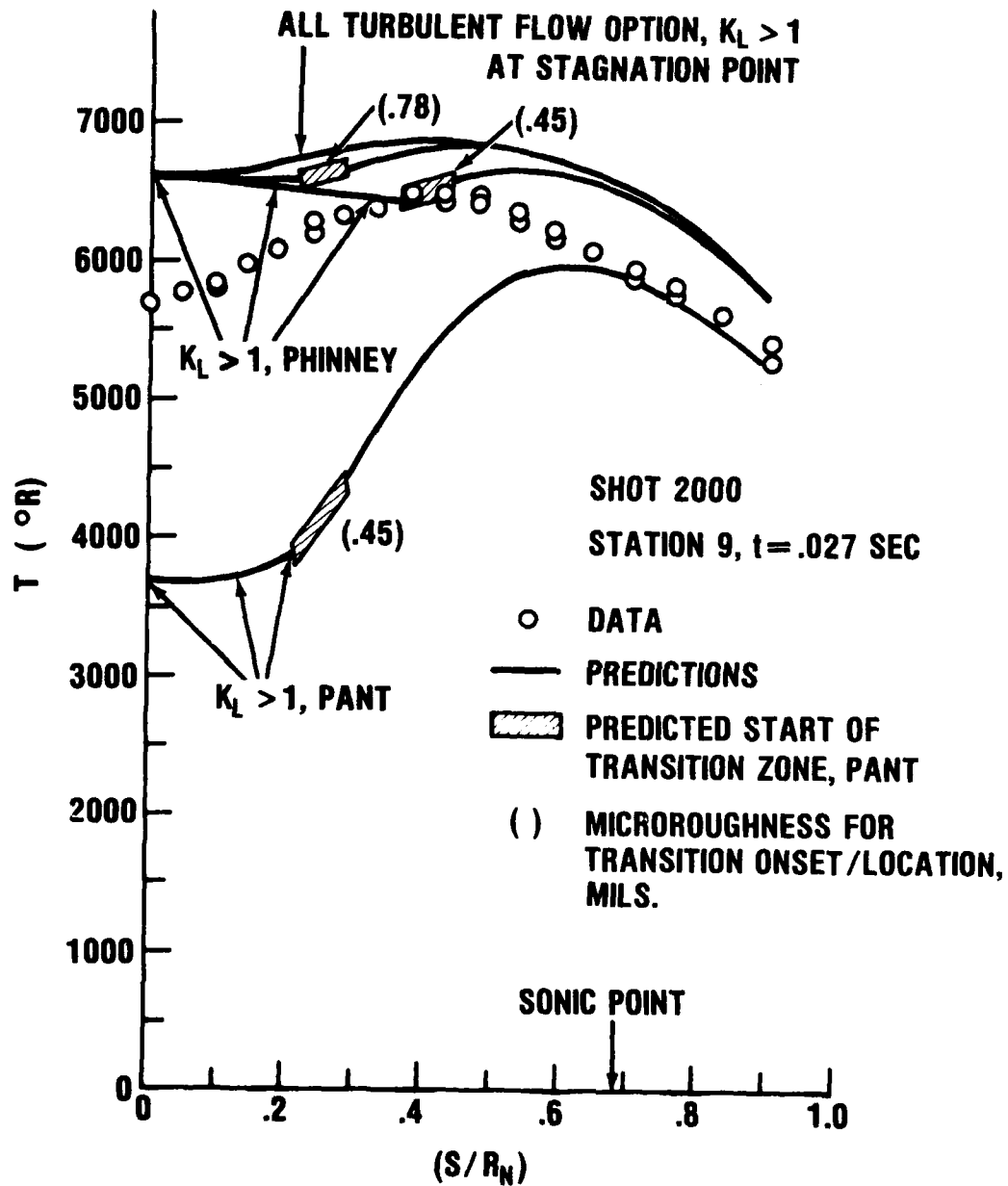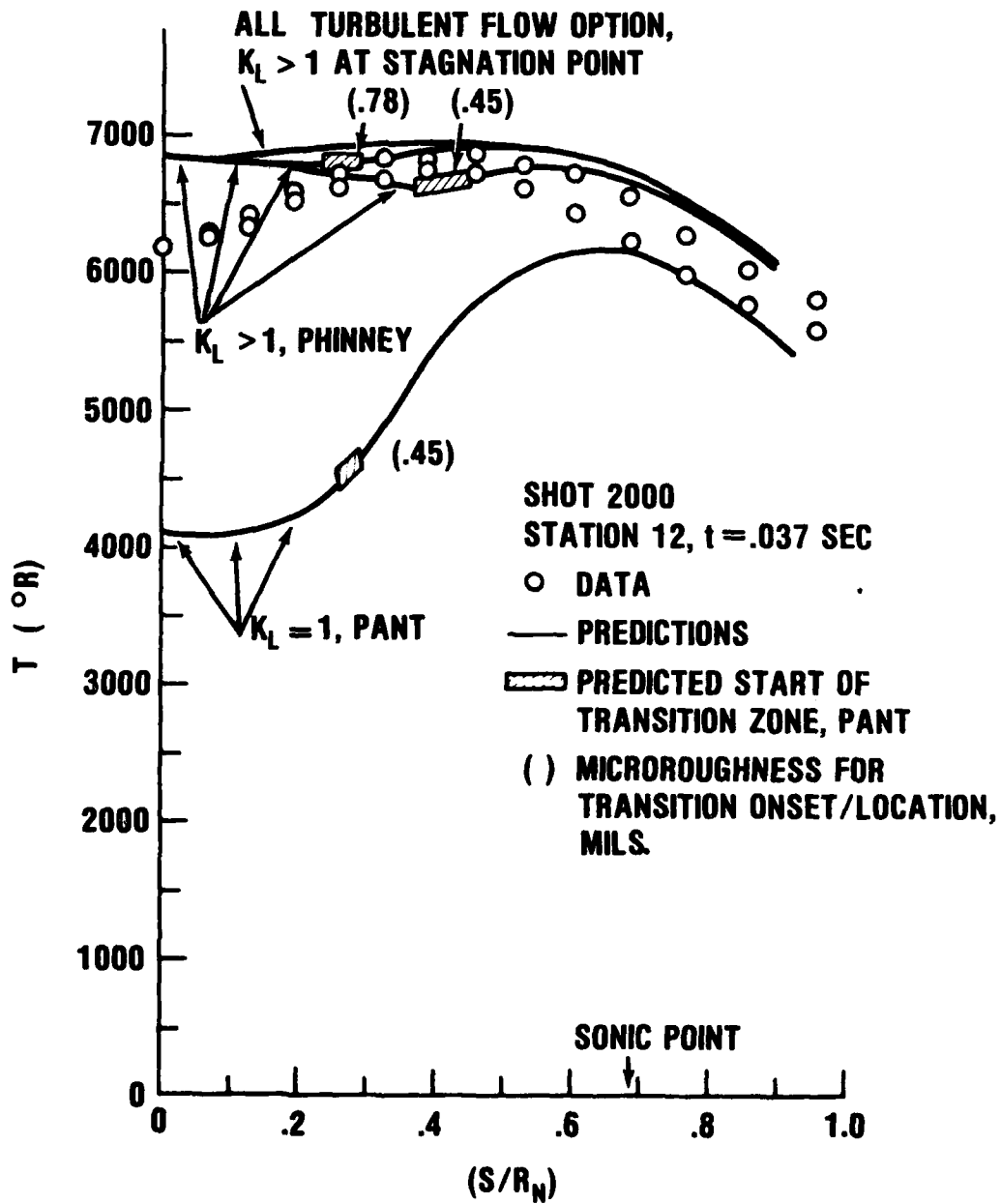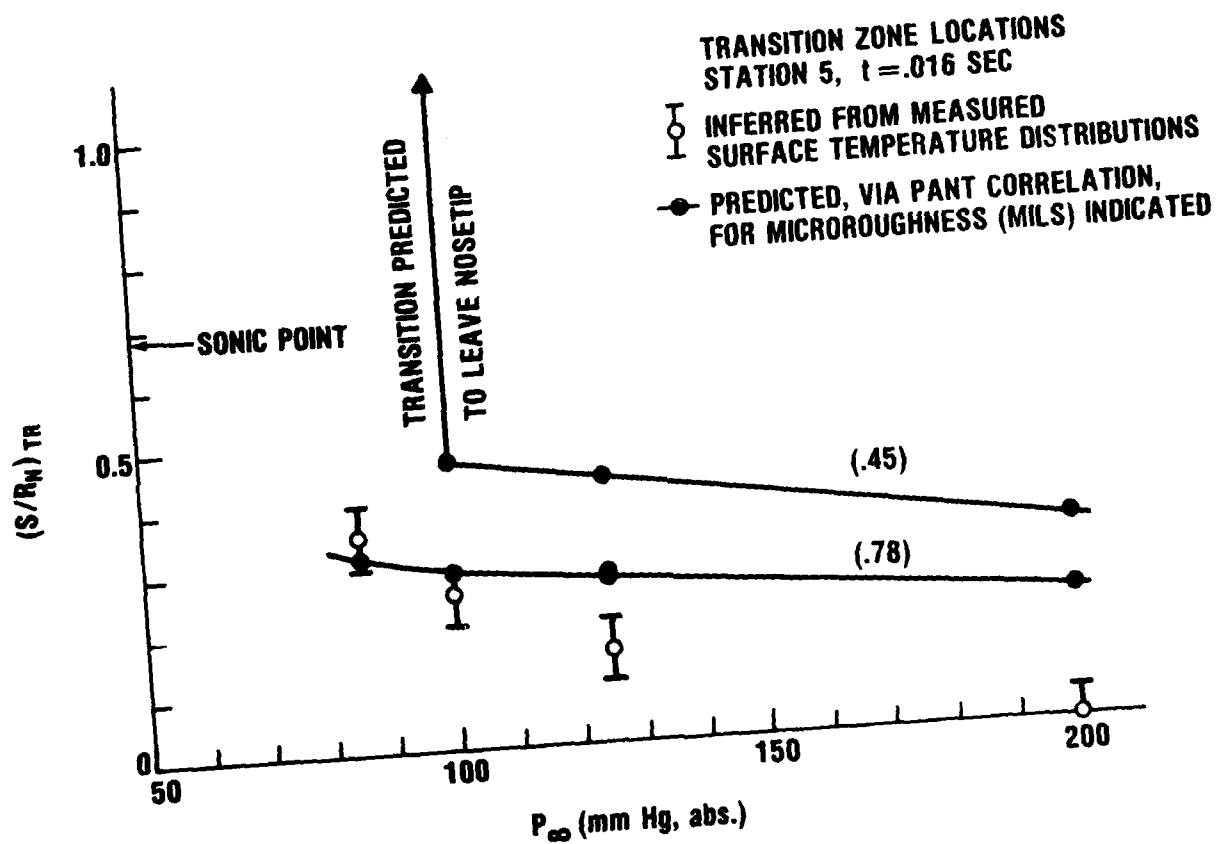
63
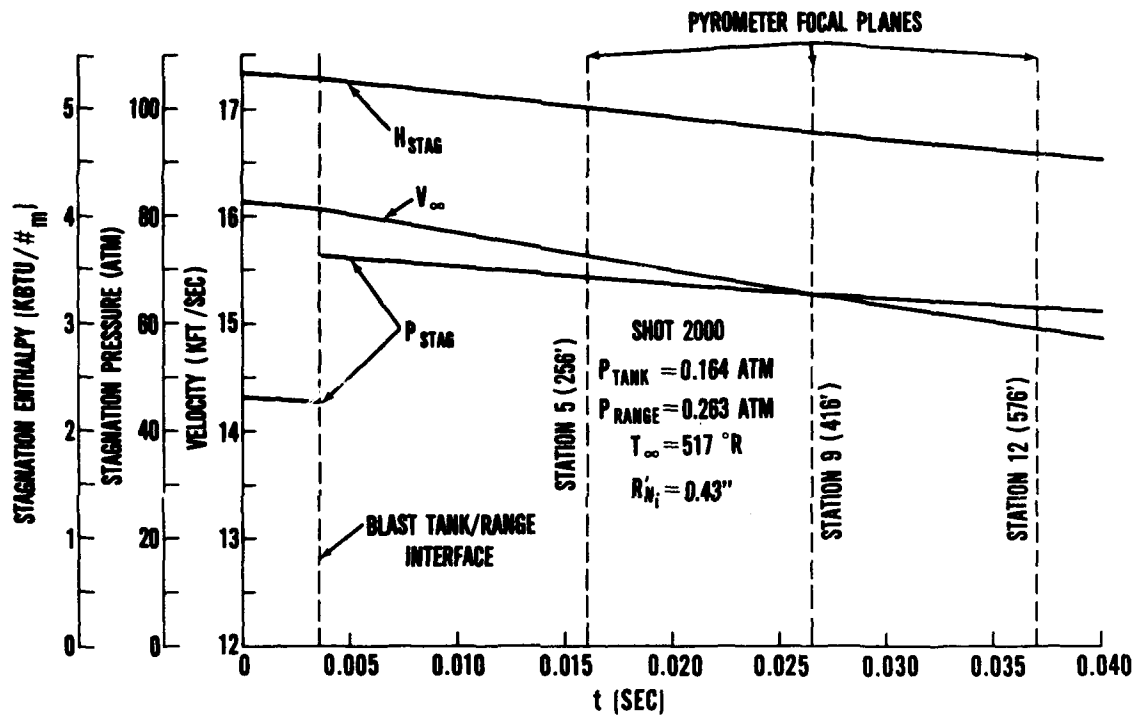
FIG. 36   AEROTHERMODYNAMIC TRAJECTORY, SHOT 2000

FIG. 37   T vs. (S/R$_n$), SHOT 2000, .016 SEC.

FIG. 38   T vs. (S/R$_n$), SHOT 2000, .027 SEC.

FIG. 39   T vs. (S/R$_n$), SHOT 2000, .037 SEC.

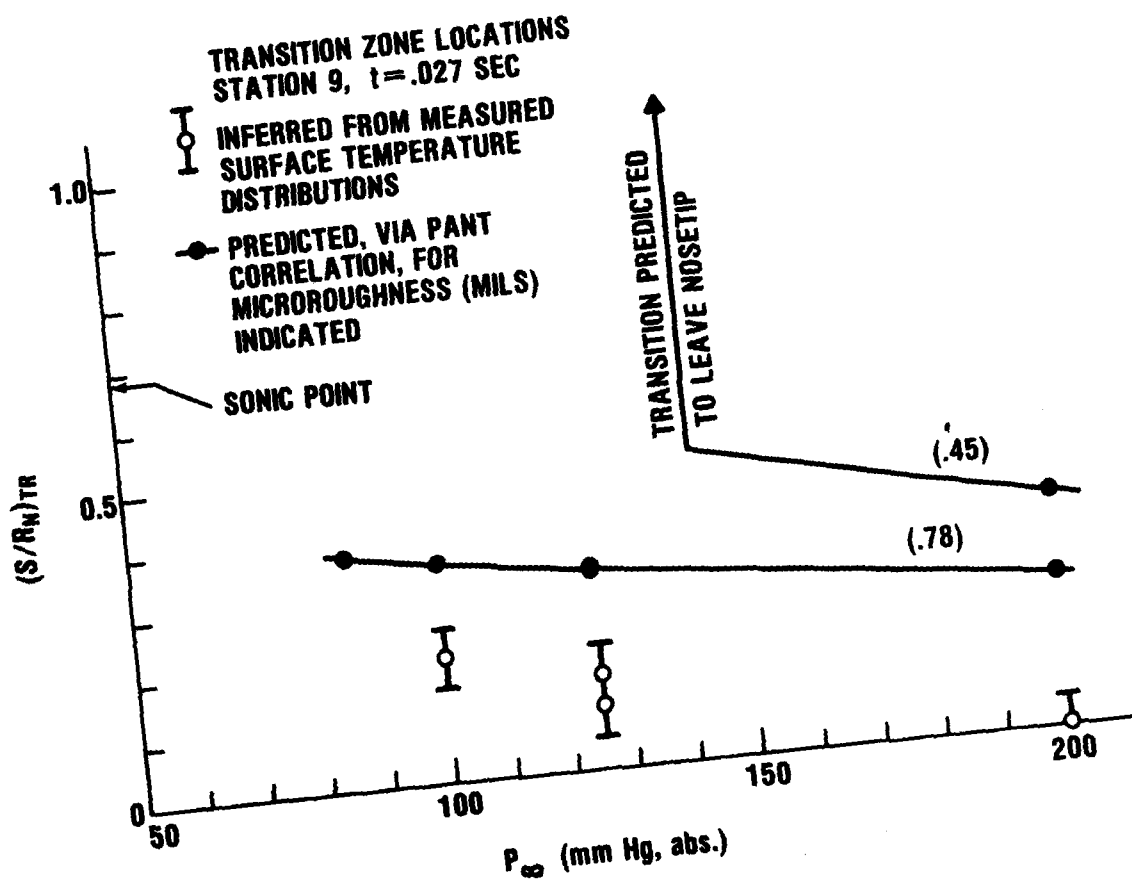FIG. 40   TRANSITION ZONE LOCATION, PANT vs. DATA, .016 SEC.

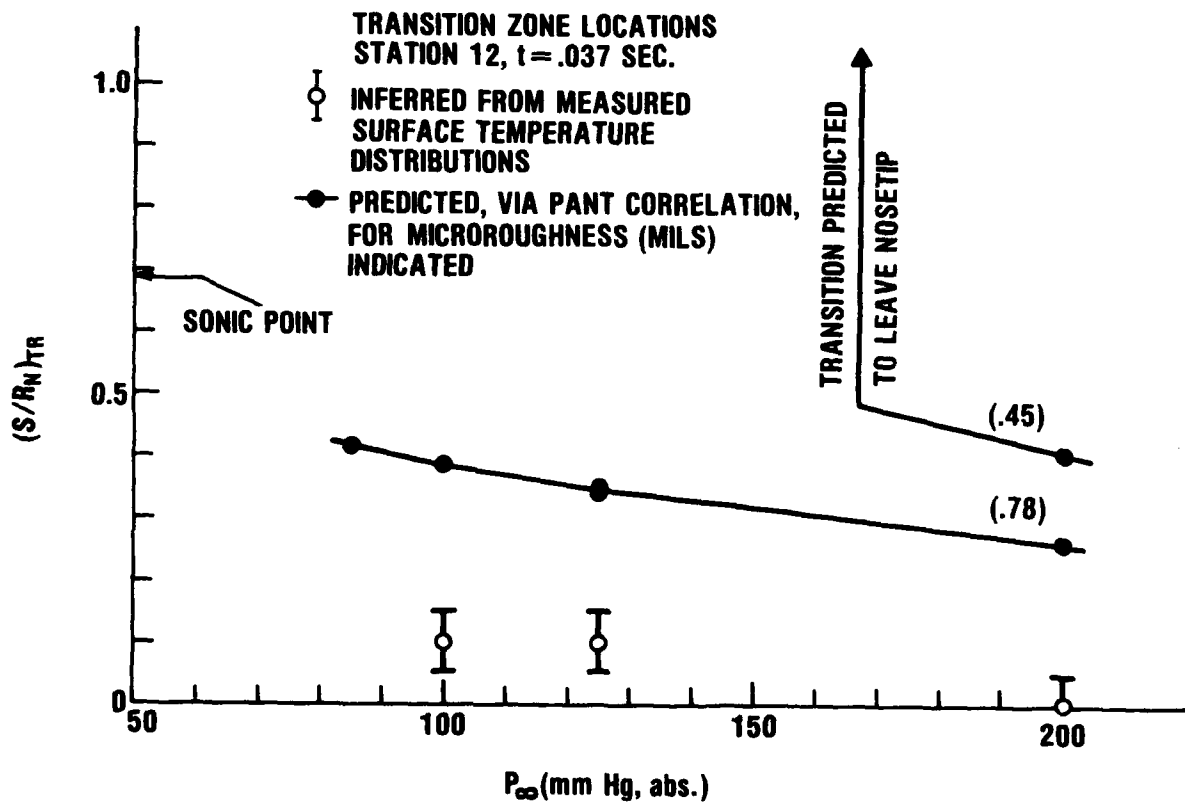FIG. 41 TRANSITION ZONE LOCATION, PANT vs. DATA, .027 SEC.

69

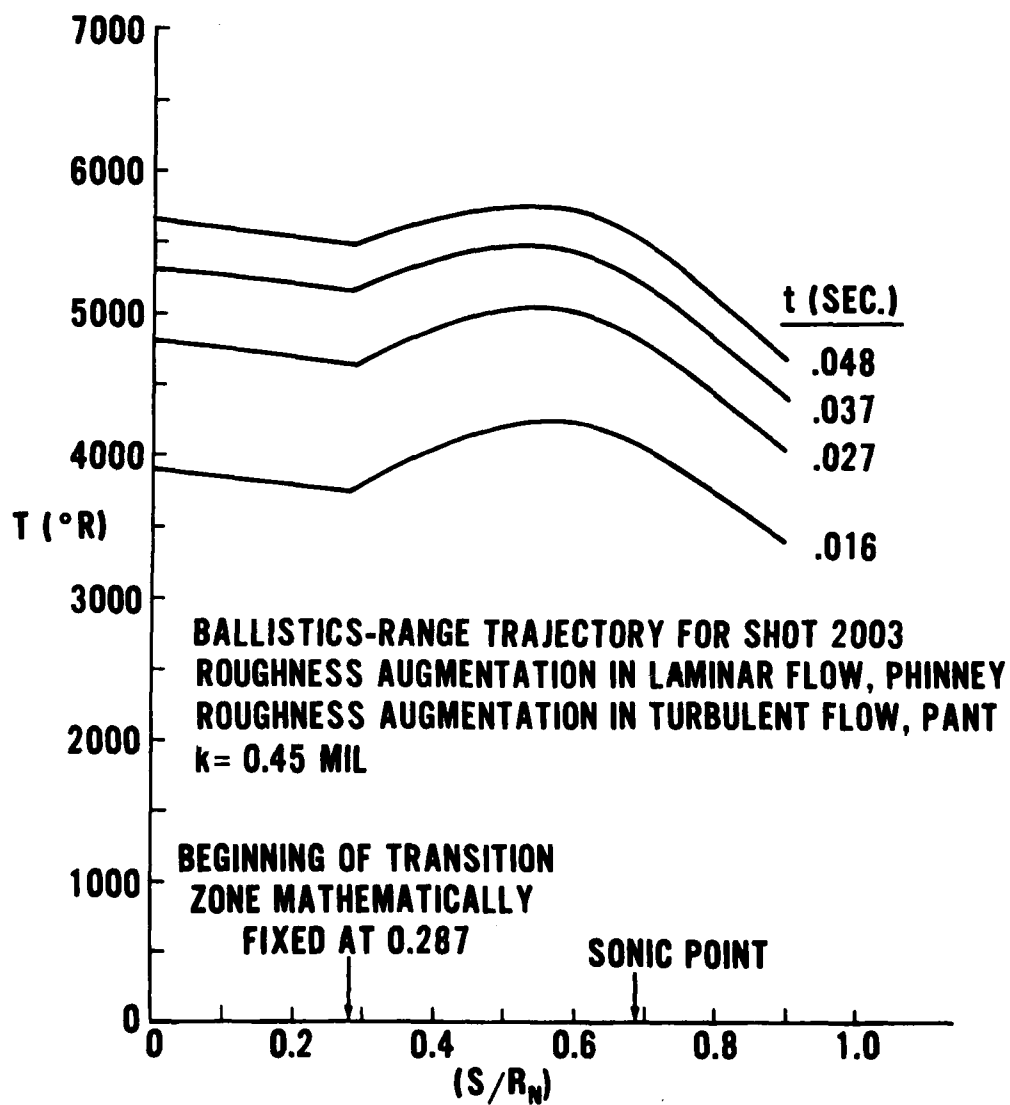FIG. 42   TRANSITION ZONE LOCATION, PANT vs. DATA, .037 SEC.

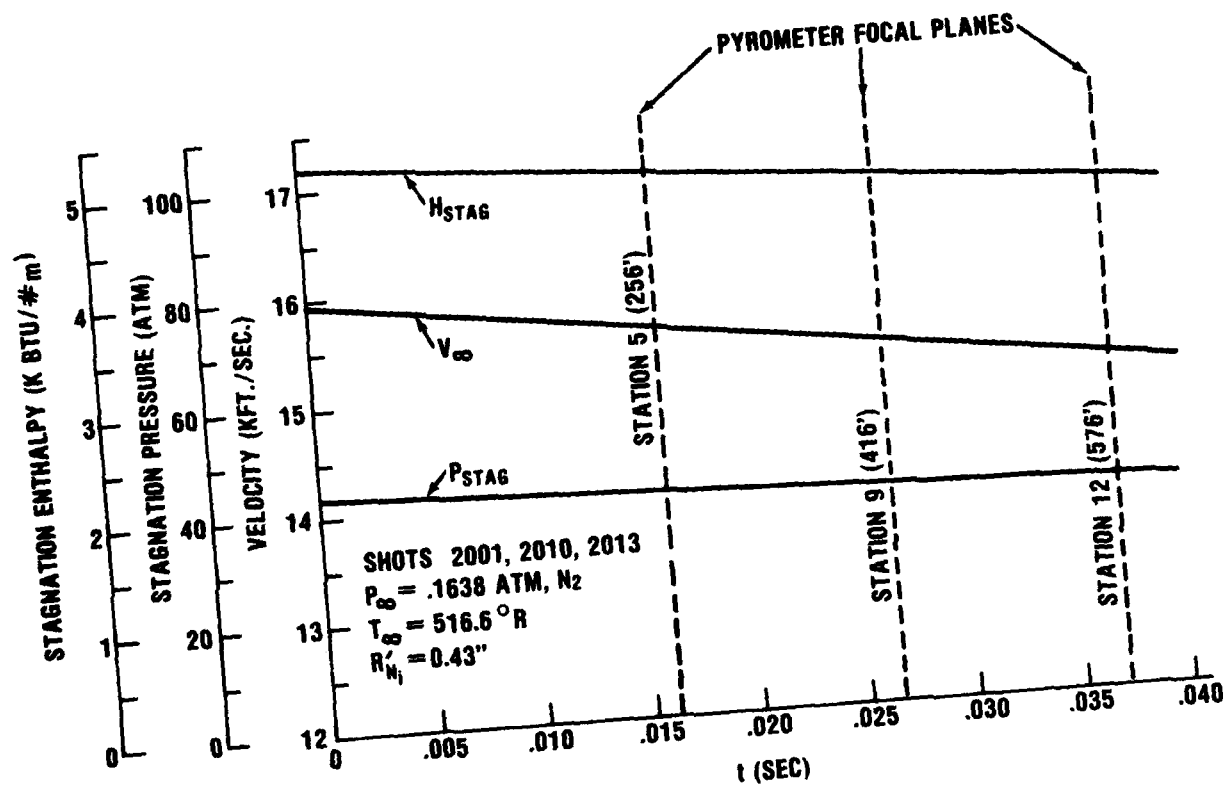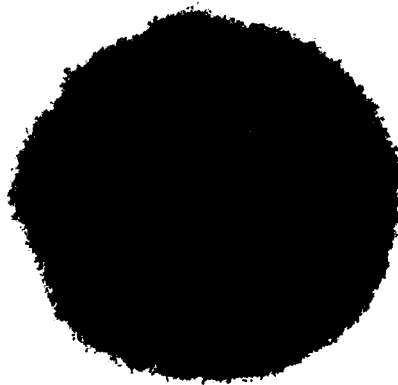FIG. 43   SENSITIVITY OF INFERRED TRANSITION ZONE LOCATION TO LATERAL CONDUCTION EFFECTS

FIG. 44   AEROTHERMODYNAMIC TRAJECTORY, SHOTS 2001, 2010, 2013, THROUGH NITROGEN

SHOT 2001 (N$_2$)
STATION 5, t = .016 SEC.

SHOT 2010 (N$_2$)
STATION 12, t = .037 SEC.
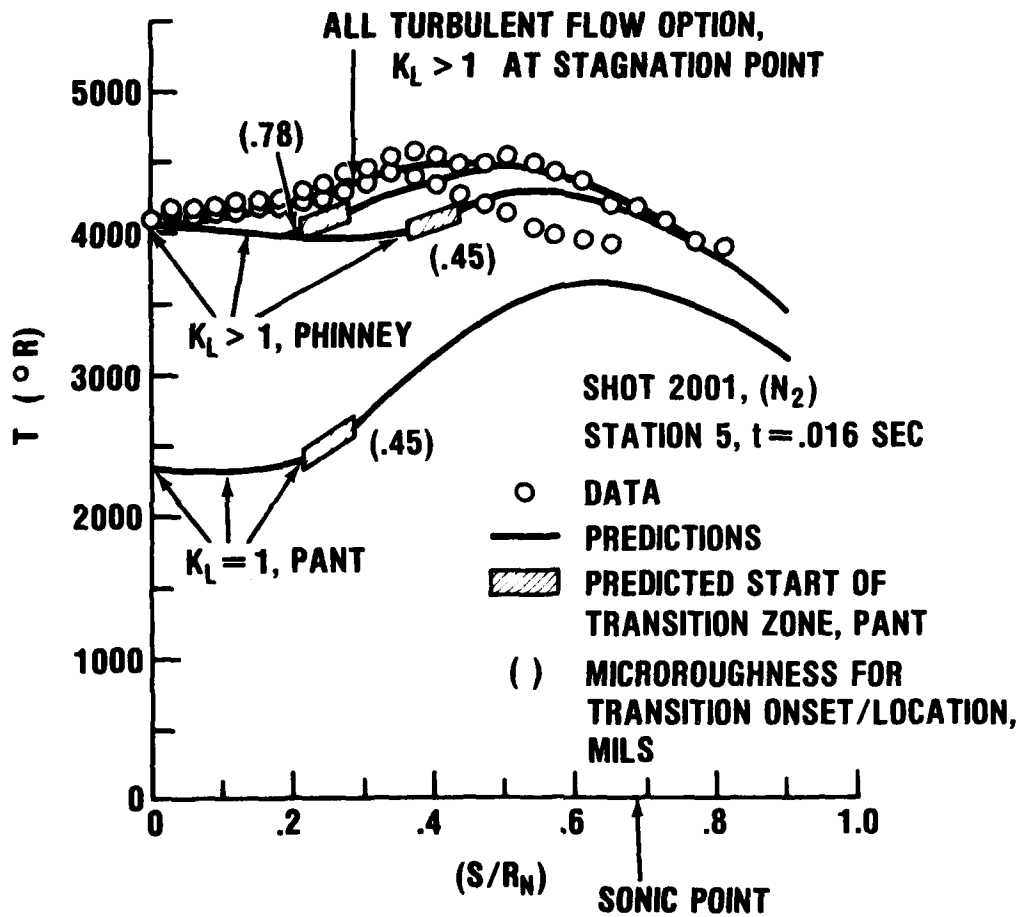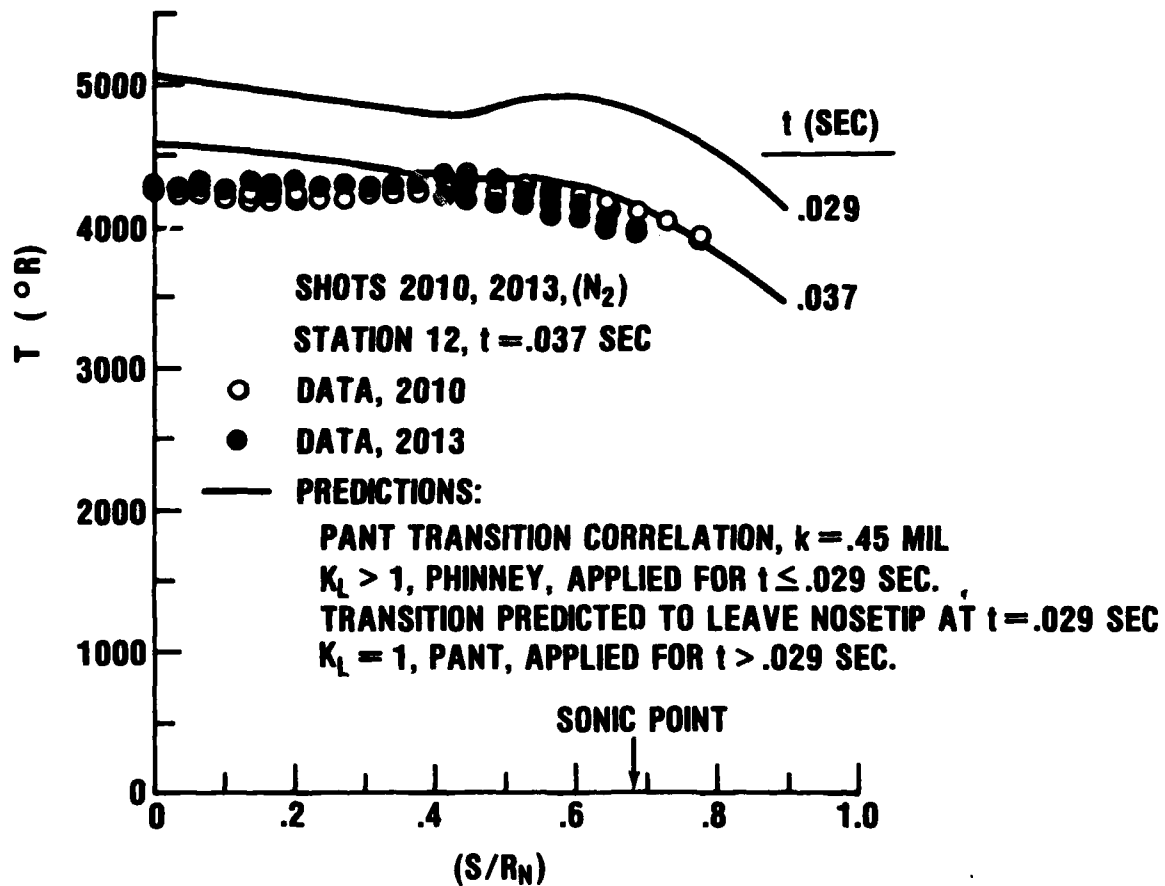
FIG. 45 DATA NEGATIVES FOR FLIGHTS THROUGH NITROGEN

73

FIG. 46   T vs. (S/R$_n$), SHOT 2001, .016 SEC.

74

FIG. 47   T vs. (S/R$_n$), SHOTS, 2010, 2013, .037 SEC.

NAVAL SURFACE WEAPONS CENTER

WHITE OAK LABORATORY

SILVER SPRING, MARYLAND 20910

To all holders of NSWC/WOL/TR 76-71   Change

Title: Boundary-Layer Transition Experiments on Pre-Ablated Graphite Nosetips in a Hyperballistics Range

Approved by Commander, NAVSURFWPNCEN   19&20 page(s)

<u>C. A. FISHER</u>
By direction   (WA-40)

This publication is changed as follows:

Page-sheet 19/20 should be replaced by the modified page-sheet 19/20 enclosed; only changes made concern use of reference (15).

Insert this change sheet between the cover and the DD Form 1473 in your copy.
Write on the cover "Change   inserted"

(i.e., the local depth of radiating gas) and subsequently computes the integral listed at the bottom of Figure 22, a measure of the local gas cap radiation (energy/unit area) can be derived. In this calculation, the one-half factor accounts for that portion of the radiant energy per unit volume directed towards the sensing instrument. A computer code for performing the above calculations was developed by Miller of AEDC and has been applied here.

Having calculated the energy per unit area radiated by the gas cap to the image converter camera, it remains to devise a procedure whereby corrections for this contribution to the data signal can be made. A relationship between energy per unit area sensed by the pyrometer and brightness temperature of the radiating source is thus required.

Figure 23 shows the energy radiated into hemispherical space by a unit area of a black ($\varepsilon = 1$) and a grey ($\varepsilon = .9$) surface, each at 7000°R, as a function of wavelength. Photocathode tube response ($S_{11}(\lambda)$) and overall pyrometer system response ($S_{11}(\lambda) \cdot W_{12}(\lambda)$) to the grey-body energy input are also shown. An integration with respect to wavelength of this lower curve yields the energy per unit area sensed by the electro-optical pyrometer system for a grey body at the specified surface temperature. Such calculations were made for both black and grey ($\varepsilon = 0.9$) surfaces over the full operating temperature range of the present pyrometer systems (both $S_{11}(\lambda)$ and $S_{20}(\lambda)$ tubes) and results are shown in Figure 24. Several points concerning this figure should be made.

First, an uncertainty in surface emissivity of the order of ten percent results in only a 30-50°K uncertainty in surface brightness temperature. Second, an equivalent blackbody brightness temperature can be defined for any computed gas cap radiation level. Third, corrections to measured surface temperatures for gas cap radiation can be made as noted below. For any specified position on the nose-tip, Figure 24 defines a radiant energy level corresponding to the measured brightness temperature. An independent calculation of local gas cap radiant energy per unit area is made, and this value is subtracted from the experimentally defined energy level. The resulting net energy level is attributed to surface radiation, and a corrected model surface temperature is thus defined.

Under conditions of the present experiment, gas-cap corrections were found to be everywhere less than $|-100^{\circ}R|$, and as such, were not applied.

---

[15]Miller, J. T., Personal Communication, Sep 1974

V   EXPERIMENTAL RESULTS VS PREDICTIONS

During the present program, a total of eight data shots were made, five in air and three in nitrogen. Nosetip images recorded during these tests were scanned and plotted according to techniques described in Section IV, D. Surface temperature distributions so obtained are presented herein as T vs (S/R_N) plots on two rays, 180° apart. Results presented in this manner give a representative indication of circumferential data spread noted for each case.

This section is subdivided into three subsections. The first summarizes results concerning roughness effects on laminar heat-transfer rates; the second and third subsections present and discuss results for flights through air (B'> 0) and nitrogen (B' = 0), respectively.

A.   Roughness Effects on Laminar Heat-Transfer Rates

As discussed in Section III, specific test conditions and instrumentation locations for the present experiment were selected based on pre-test calculations of nosetip transient thermal response. Since the nosetip boundary-layer transition correlation in question possesses a strong wall-temperature dependence, predicted flight times to transition offset are obviously dependent on methods used to calculate surface heat-transfer rates. Results of the present experiment substantiated use of equation (3) to model roughness effects on laminar heat-transfer rates.

Figure 25 summarizes these results by comparing stagnation point temperatures, predicted via the PANT[1] and Phinney[5] correlations, with measured values. All data shown in Figure 25 were obtained under conditions which resulted in the presence of a transition zone within the subsonic flow region of the nosetip.

The PANT correlation predicted no augmentation (K_L = 1.0) under present test conditions; stagnation point temperatures so predicted were consistently 30 to 50 percent below measured values. Phinney's correlation predicted augmentation factors of ~1.8 $\leq K_L \leq$ ~2.3; stagnation point temperatures so predicted were within ±10% for 10 of the 14 data points shown, and within ±12-1/2% for 12 of these same 14 measured values.

B.   Flights Through Air

Flights were conducted through air at freestream static pressure levels .112 $\leq P_\infty \leq$ .263 atm. (~30 $\leq P_{STAG} \leq$ ~70 atm.), i.e., under conditions ranging from predicted transition offset prior to the first data monitoring station, to conditions under which a transition zone was predicted to exist on the nosetip throughout the entire monitored portion of its flight (recall Table 1).